

Suzaku OBSERVATIONS OF THE DIFFUSE X-RAY EMISSION ACROSS THE FERMI BUBBLES' EDGES

J. KATAOKA^{1,2}, M. TAHARA¹, T. TOTANI³, Y. SOFUE³, Ł. STAWARZ^{4,5}, Y. TAKAHASHI¹, Y. TAKEUCHI¹,
H. TSUNEMI⁶, M. KIMURA⁴, Y. TAKEI⁴, C. C. CHEUNG⁷, Y. INOUE⁸, AND T. NAKAMORI⁹

Draft version July 7, 2018

ABSTRACT

We present *Suzaku* X-ray observations along two edge regions of the Fermi Bubbles, with eight $\simeq 20$ ksec pointings across the northern part of the North Polar Spur (NPS) surrounding the north bubble and six across the southernmost edge of the south bubble. After removing compact X-ray features, diffuse X-ray emission is clearly detected and is well reproduced by a three-component spectral model consisting of unabsorbed thermal emission (temperature $kT \simeq 0.1$ keV) from the Local Bubble (LB), absorbed $kT \simeq 0.3$ keV thermal emission related to the NPS and/or Galactic Halo (GH), and a power-law component at a level consistent with the cosmic X-ray background. The emission measure (EM) of the 0.3 keV plasma decreases by $\simeq 50\%$ toward the inner regions of the north-east bubble, with no accompanying temperature change. However, such a jump in the EM is not clearly seen in the south bubble data. While it is unclear if the NPS originates from a nearby supernova remnant or is related to previous activity within/around the Galactic Center, our *Suzaku* observations provide evidence suggestive of the latter scenario. In the latter framework, the presence of a large amount of neutral matter absorbing the X-ray emission as well as the existence of the $kT \simeq 0.3$ keV gas can be naturally interpreted as a weak shock driven by the bubbles' expansion in the surrounding medium, with velocity $v_{\text{exp}} \sim 300$ km s⁻¹ (corresponding to shock Mach number $\mathcal{M} \simeq 1.5$), compressing the GH gas to form the NPS feature. We also derived an upper limit for any non-thermal X-ray emission component associated with the bubbles and demonstrate, that in agreement with the findings above, the non-thermal pressure and energy estimated from a one-zone leptonic model of its broad-band spectrum, are in rough equilibrium with that of the surrounding thermal plasma.

Subject headings: acceleration of particles — cosmic rays — Galaxy: center — Galaxy: halo — X-rays: ISM

1. INTRODUCTION

The Large Area Telescope (LAT; Atwood et al. 2009) onboard the *Fermi* satellite is a successor to EGRET onboard the Compton Gamma-ray Observatory (Hartman et al. 1999), with much improved sensitivity and resolution over a broader energy range. Along with the GeV detections of various γ -ray source types (e.g., Nolan et al. 2012), yet another important LAT discovery concerns the large-scale γ -ray structure, the so-called “Fermi Bubbles,” extending for about 50° (or 8.5 kpc) above and below the Galactic Center (GC), with a longitudinal width $\sim 40^\circ$ (Dobler et al. 2010; Su et al. 2010). It has been suggested that these bubbles have relatively sharp edges and are symmetric with respect to the Galactic plane and the minor axis of the Galactic disk. The γ -ray emission associated with the bubbles is characterized by a hard spectrum with the differential γ -ray spectral photon index $\Gamma \simeq 2$;

no significant spectral or total intensity variations have been found within the structure, with the exception of some hints for an additional substructure consisting of a cocoon and jet-like features extending in the north-west and south-east directions (Su & Finkbeiner 2012). The sharp edges may suggest the presence of a shock at the bubbles' boundaries. If however this is the case, and if the shock is the sole acceleration site of the γ -ray emitting particles, both the observed flat intensity profile and the uniformly hard spectrum within the bubbles' interior extending for about 10 kpc, seem rather difficult to explain.

Importantly, the γ -ray emission of the bubbles is spatially correlated with the flat-spectrum microwave excess known as the “WMAP haze.” The haze, recently confirmed with *Planck* observations (Planck Collaboration et al. 2013), is characterized by a spherical morphology with a radius ~ 4 kpc centered at the GC, and is visible up to at least $|b| \simeq 30^\circ$ (Finkbeiner 2004; Dobler & Finkbeiner 2008). The entire microwave continuum of the haze is consistent with a power-law distribution with spectral index $\alpha = 0.5$, and is best interpreted as synchrotron emission from a flat-spectrum population of cosmic ray (CR) electrons. Hence it has been argued that the WMAP haze and the Fermi bubbles are linked, and that the γ -ray emission of the bubbles is simply the inverse-Compton scattering of the cosmic microwave background (IC/CMB) emission from the same electron population producing the observed microwave synchrotron excess (e.g., Su et al. 2010; Mertsch & Sarkar 2011). In this model, the smaller latitudinal extension of the WMAP haze may be due to a decrease in the magnetic field intensity with increasing latitude. However, the expected polarization of the

¹ Research Institute for Science and Engineering, Waseda University, 3-4-1, Okubo, Shinjuku, Tokyo 169-8555, Japan

² email: kataoka.jun@waseda.jp

³ Department of Astronomy, The University of Tokyo, Bunkyo-ku, Tokyo 113-0033, Japan

⁴ Institute of Space and Astronautical Science, JAXA, 3-1-1 Yoshinodai, Chuo-ku, Sagami, Kanagawa 252-5210, Japan

⁵ Astronomical Observatory, Jagiellonian University, ul. Orla 171, 30-244 Kraków, Poland

⁶ Department of Earth and Space Science, Osaka University, Osaka 560-0043, Japan

⁷ Space Science Division, Naval Research Laboratory, Washington, DC 20375, USA

⁸ Kavli Institute for Particle Astrophysics and Cosmology, Stanford University, Stanford, CA 94305, USA

⁹ Department of Physics, Faculty of Science, Yamagata University, 990-8560, Japan

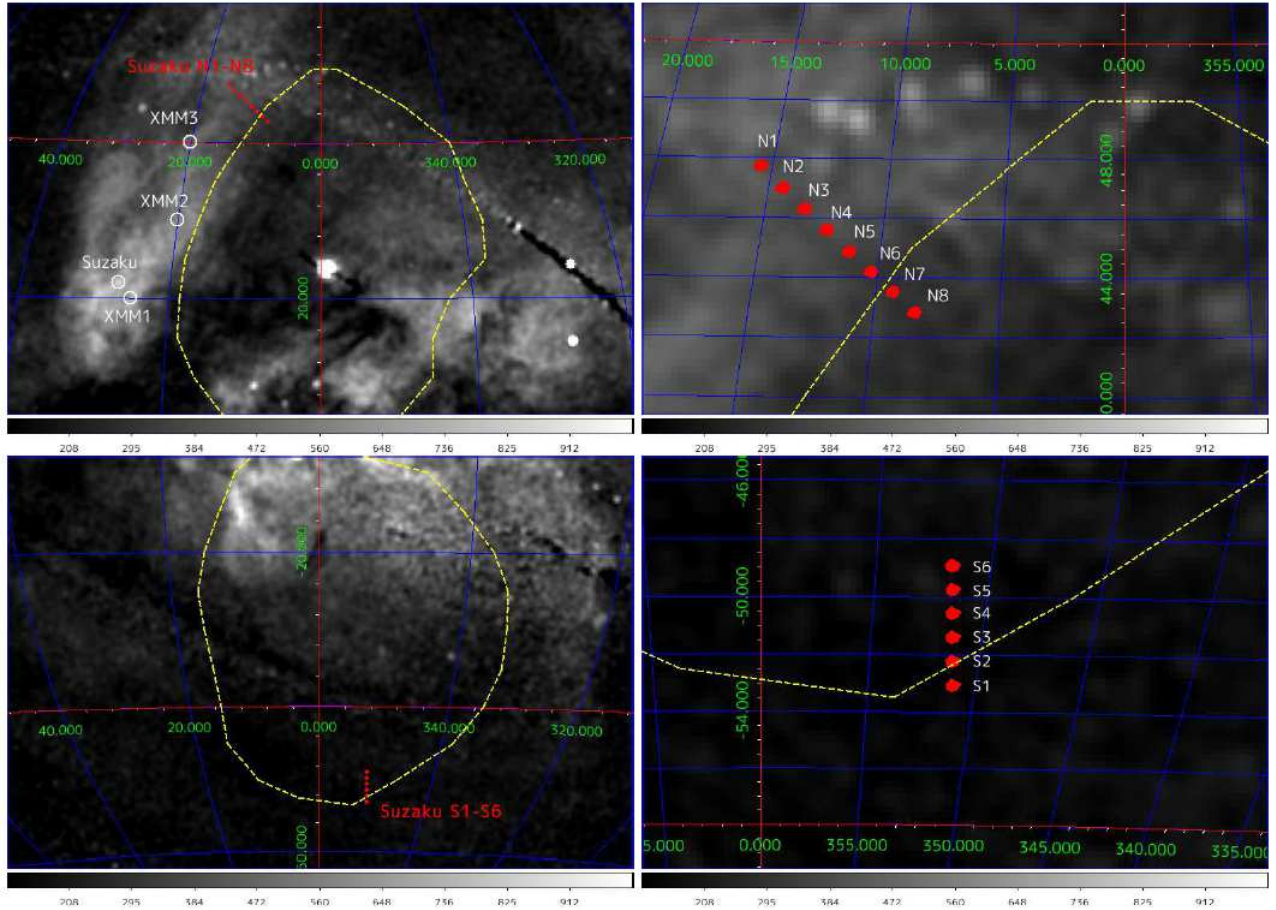


FIG. 1.— *Suzaku* XIS field of views (red) overlaid with the *ROSAT* 0.75 keV image for the series of north-east and southern observations of the Fermi Bubbles. All the figures are shown in Galactic coordinates. Yellow dashed lines indicate the boundary of the bubbles, as suggested in Su et al. (2010). *Top-left*: X-ray image of the north-east bubble, along with the focal centers of previous *Suzaku* and *XMM* observations of the NPS (Willigale et al. 2003; Miller et al. 2008). *Top-right*: A close-up of the north-east edge of the bubble. *Bottom-left*: X-ray image of the southern bubble. *Bottom-right*: A close-up of the southern edge of the bubble. The gray scale ranges of the *ROSAT* images (units of 10^{-6} cts s^{-1} arcmin $^{-2}$) are indicated at the bottom of each panel.

haze was not detected in the most recent accumulation of the WMAP-7 year data (Gold et al. 2011), indicating that the magnetic field in the bubbles is heavily tangled, or an alternative emission mechanism is at work. In this context, some authors argued that the bubbles/haze structure may be explained as rather being due to a population of relic CR protons and heavier ions injected about $\simeq 10$ Gyr years ago during the outburst of a high areal density star-forming activity around the GC (Crocker & Aharonian 2011).

At X-ray frequencies, the *ROSAT* all-sky survey (RASS) provides full-sky images with FWHM $12'$ at photon energies in the $0.5 - 2$ keV range (Snowden et al. 1995). Hints of signatures of the entire north bubble structure can be noted in the *ROSAT* map (e.g., Su et al. 2010, Figs. 18 & 19 therein), as well as two sharp edges in the south that trace the Fermi bubble below the Galactic disk (e.g., Fig. 1 in Wang 2002; Fig. 6 in Bland-Hawthorn & Cohen 2003; also, Figs. 18 & 19 in Su et al. 2010). Particularly noteworthy is a prominent Galactic feature called the North Polar Spur (NPS) seen in the 0.75 keV (*R45* band) map, a large region of enhanced soft X-ray emission projected above the plane of the Galaxy which coincides with a part of the radio Loop I structure. Sofue (2000, and references therein) interpreted the NPS as a large-scale outflow from the GC with a corresponding total energy of $\sim 10^{55} - 10^{56}$ erg released on a timescale of $\sim 10^7$ yr.

This idea was questioned by several authors who argued that the NPS and the rest of the Loop I may instead be a nearby supernova remnant (Berkhuijsen et al. 1971) or may be related to the wind activity of the Scorpio-Centaurus OB association located at a distance of 170 pc (Egger & Aschenbach 1995). While the GC scenario seems more plausible in view of the recent discovery of the Fermi bubbles (Su et al. 2010), the distance and origin of the NPS is still under debate, and we discuss this issue in more depth in this paper (Section 4.2).

Motivated by the substantial observational and theoretical progress recently made toward understanding the nature and origin of the large-scale structures extending above and below the GC regions, particularly with the discovery of the Fermi Bubbles, we conducted *Suzaku* X-ray observations of high-Galactic latitude regions ($43^\circ < |b| < 54^\circ$) positioned across the north-east and the southern-most edges of the bubbles. In Section 2, we describe the details of the *Suzaku* observations and data reduction procedures. The results of the analysis are given in Section 3, including the detailed spectral modeling and images obtained within the $0.4 - 10$ keV range. Here we concentrated on the analysis of the diffuse emission and assumed all the relatively bright compact X-ray features detected at $\gtrsim 5\sigma$ level are most likely background active galactic nuclei (AGN) or galaxies unrelated to the Galactic Halo (GH) and/or the NPS. Some information regarding

TABLE 1
Suzaku OBSERVATION LOG

ID	start time (UT in 2012)	stop time (UT in 2012)	R.A. [$^{\circ}$] ^a	DEC [$^{\circ}$] ^b	l [$^{\circ}$] ^c	b [$^{\circ}$] ^d	Exposure [ksec] ^e
Bubble North							
N1	Aug 08 10:23	Aug 08 23:03	233.401	9.076	15.480	47.714	20.0
N2	Aug 07 23:41	Aug 08 10:22	233.623	8.079	14.388	47.011	18.3
N3	Aug 07 10:31	Aug 07 23:40	233.834	7.087	13.321	46.308	20.4
N4	Aug 06 23:20	Aug 07 10:30	234.034	6.098	12.280	45.606	19.0
N5	Aug 05 23:04	Aug 06 09:33	234.250	5.090	11.255	44.871	17.2
N6	Aug 06 09:34	Aug 06 23:18	234.405	4.131	10.263	44.204	22.0
N7	Aug 08 23:06	Aug 09 10:20	234.551	3.174	9.291	43.537	19.4
N8	Aug 09 10:21	Aug 09 23:53	234.713	2.200	8.334	42.838	13.5
Bubble South							
S1	Apr 19 14:11	Apr 20 02:44	332.668	-46.192	351.010	-53.100	20.9
S2	Apr 19 03:15	Apr 19 14:10	331.474	-46.348	351.149	-52.265	13.2
S3	Apr 18 04:59	Apr 18 16:10	330.278	-46.492	351.281	-51.432	13.5
S4	Apr 17 16:40	Apr 18 04:58	329.080	-46.624	351.406	-50.602	24.7
S5	Apr 18 16:12	Apr 19 03:12	327.882	-46.743	351.525	-49.775	21.0
S6	Apr 20 02:47	Apr 20 14:25	326.683	-46.851	351.638	-48.950	12.4

NOTE. — ^a: Right ascension of *Suzaku* pointing center in J2000 equinox.

^b: Declination of *Suzaku* pointing center in J2000 equinox.

^c: Galactic longitude of *Suzaku* pointing center.

^d: Galactic latitude of *Suzaku* pointing center.

^e: *Suzaku* XIS exposure in ksec.

these compact X-ray features are provided in the Appendix, along with the details of our further investigation concerning the data analysis. In Section 4 we summarize our findings and discuss the expansion of the bubbles and their interaction with the GH gas. We compared the obtained *Suzaku* results with RASS observations, thus providing guidance for future high-sensitivity all-sky X-ray studies with instruments like *MAXI* (Matsuoka et al. 2009) or *eROSITA* (Merloni et al. 2012). We also revisit the widely debated issue concerning the origin of and the distance to the NPS. We argue that the NPS is formed by plasma which has been compressed and heated by a weak shock driven in the GH environment by the expanding bubbles. Finally, we discuss the energy and pressure balance between the thermal and non-thermal plasma components within the regions of interest by means of modeling the spectral energy distribution (SED) of the bubbles and of the surrounding medium as probed with the *Suzaku* data. Throughout, unless otherwise noted, all statistical uncertainties reported in the paper are at the 1σ level.

2. OBSERVATIONS AND DATA REDUCTION

2.1. *Suzaku* Observations

We conducted *Suzaku* observations of the north-east and southern edges of the Fermi Bubbles as a part of an AO7 program in 2012 with a total (requested) duration of 280 ks. The campaign consisted of 14 observations, $\simeq 20$ ksec each, consisting of eight pointings overlapping with the north-east bubble edge and across part of the NPS, with the remaining six pointings over the southern edge of the south bubble. Table 1 summarizes the times of the exposures, directions of the pointing centers (in both equatorial and Galactic coordinates), and the effective duration of each pointing. The angular offset between each pointing was 1.02 deg for the north-east edge and 0.88 deg for the south bubble edge. Because of the overlap with the NPS, we obtained additional pointings in the northern bubble region (spacing them out more widely) than in the southern bubble in order to sample a wider angular range.

The *Suzaku* satellite (Mitsuda et al. 2007) carries four sets

of X-ray telescopes (XRT; Serlemitsos et al. 2007), each with a focal-plane X-ray CCD camera (X-ray Imaging Spectrometer, XIS; Koyama et al. 2007) sensitive to photons in the energy range of 0.3 – 12 keV. Despite the relatively large point spread function (PSF) of the XRT with a half-power diameter of $\simeq 2.0'$, *Suzaku* is the ideal instrument for the intended study because it provides a low and stable Non X-ray Background (NXB), particularly suitable for investigating extended and low surface-brightness X-ray sources (Mitsuda et al. 2007; Tawa et al. 2008). Three spectrometers (XIS 0, 2, 3) have front-illuminated (FI) CCDs, while the XIS 1 utilizes a back-illuminated (BI) CCD. Each XIS covers a $18' \times 18'$ region on the sky. Because of an anomaly in 2006 November, the operation of the XIS 2 was terminated, thus here we use only the remaining three CCDs. The cameras were operated in the normal full-frame clocking mode with the 3×3 or 5×5 editing mode. Although *Suzaku* carries also a hard X-ray detector (HXD; Takahashi et al. 2007), hereafter we do not use the data collected by its PIN and GSO instruments. Figure 1 shows our *Suzaku* XIS fields of view overlaid onto the *ROSAT* 0.75 keV image for the series of north-east and southern observations of the Fermi Bubbles. Yellow dashed curves indicate the boundary of the Fermi Bubbles, as proposed in Su et al. (2010). Note that at lower northern Galactic latitudes, the relatively bright NPS regions have already been targeted with *Suzaku* and *XMM* (Willingale et al. 2003; Miller et al. 2008) and the corresponding focal centers of these archival observations are denoted in the figure by white circles.

2.2. XIS Analysis

For the XIS, we analyzed the screened data reduced using the *Suzaku* software version 1.2. The reduction followed the prescriptions given in ‘*The Suzaku Data Reduction Guide*’ (also known as ‘*The ABC Guide*’) provided by the *Suzaku* guest observer facility at NASA/GSFC.¹⁰ The screening was

¹⁰ <http://suzaku.gsfc.nasa.gov/docs/suzaku/analysis/abc>,
<http://www.astro.isas.jaxa.jp/suzaku/analysis>.

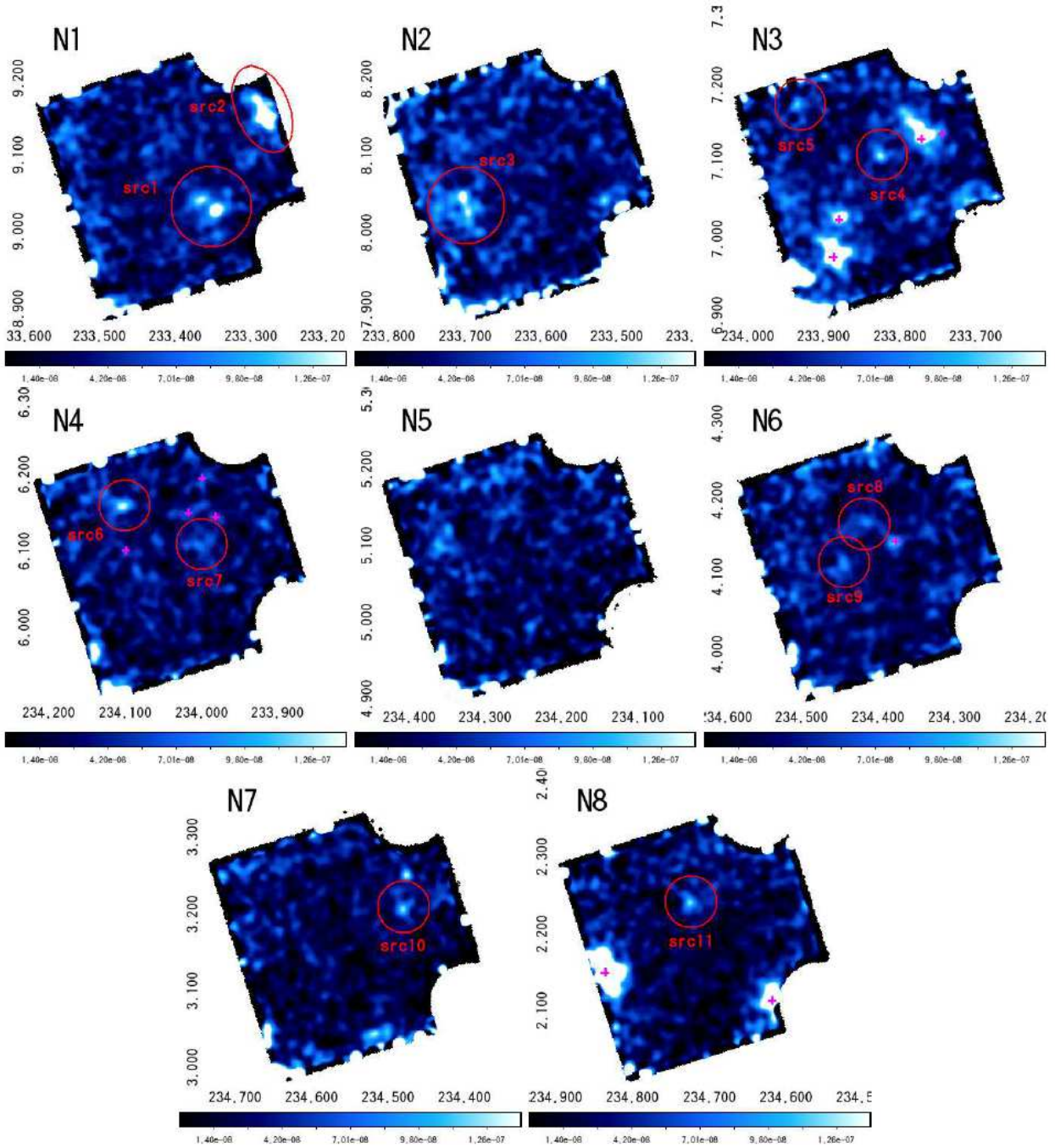


FIG. 2.— The 0.4 – 10 keV XIS (XIS 0+3) images of the north-east *Suzaku* fields N1–N8, after vignetting correction and subtraction of the “non-X-ray background”. Uncatalogued X-ray features detected above $\approx 5\sigma$ level are denoted as src1–11; the corresponding source extraction regions are denoted by red circles/ellipses. The size of the source extraction regions were changed between 1” and 2” to avoid contaminations from nearby sources. Also we assumed an elliptical region for src2 because it is situated at the corner of the CCD and hence appears elongated along the direction of the CCD edge. The bright X-ray features that are catalogued sources are marked with magenta crosses. All the figures are shown in Equatorial coordinates (J2000).

based on the following criteria: (1) only ASCA-grade 0, 2, 3, 4, 6 events were accumulated with hot and flickering pixels removed from the XIS image using the CLEAN SIS script (Day et al. 1998); (2) the time interval after the passage of the South Atlantic Anomaly (T_SAA_HXD) greater than 500 s; (3) targets were located at least 5° and 20° above the rim of the Earth (ELV) during night and day, respectively. In addition, we also selected the data with a cutoff rigidity (COR) larger than 6 GV. After this screening, the sum of the net expo-

sure for good time intervals was 149.8 ks for the N1–N8 and 105.7 ks for the S1–S6 pointings (see Table 1). In the reduction and the analysis of the *Suzaku* XIS data, the HEADAS software version 6.12 and the calibration databases (CALDB) released on 2012 July 11 were used, all kindly provided by the XIS instrumental team. The XIS cleaned event dataset was obtained in the combined 3×3 and 5×5 edit modes using XSELECT.

We extracted the XIS images from only the two FI CCDs

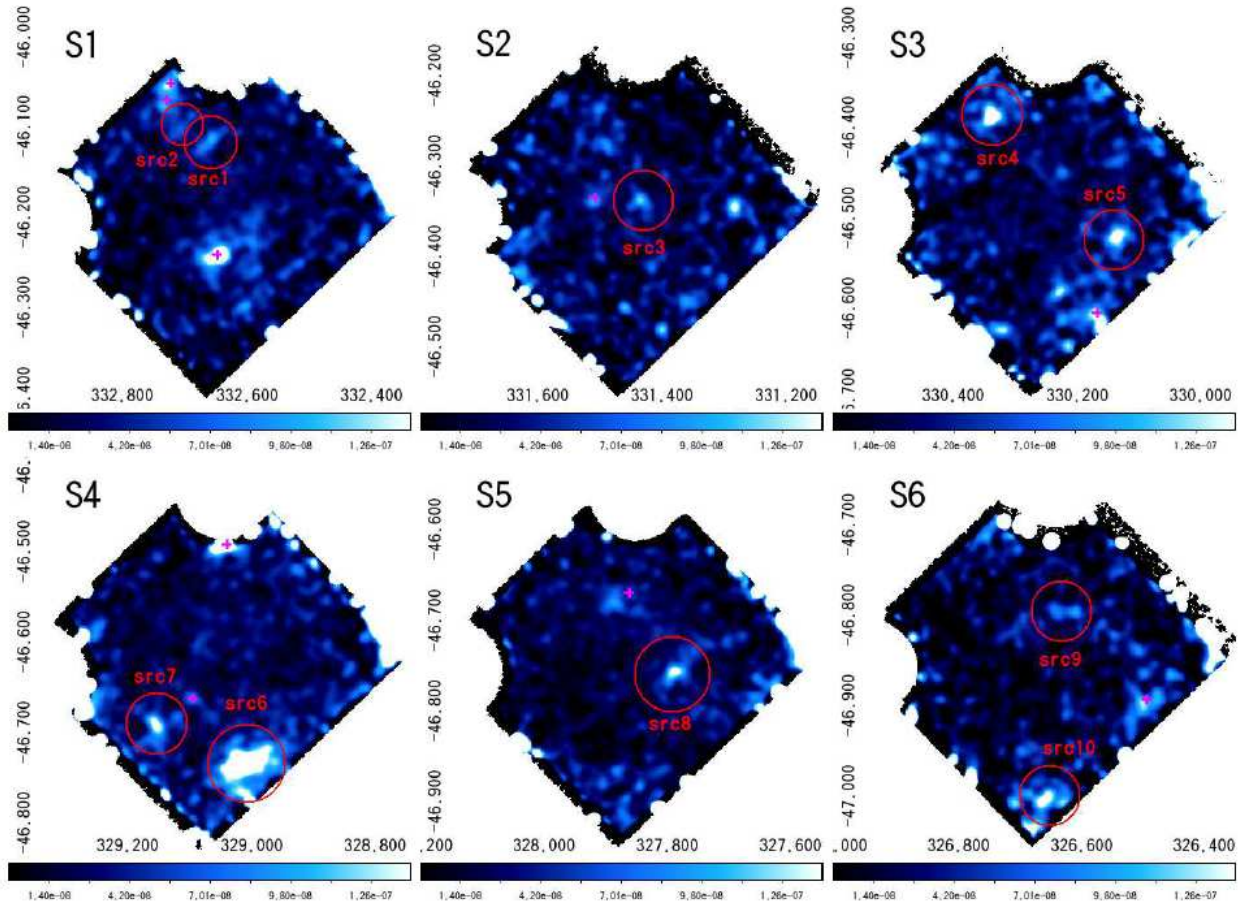


FIG. 3.— As in figure 2, but for the southern bubble *Suzaku* fields S1–S6.

(XIS 0, XIS 3) because the BI CCD (XIS1) has lower imaging quality due to its higher instrumental background. The XIS images were made within three photon energy ranges of 0.4 – 10 keV, 0.4 – 2 keV, and 2 – 10 keV. In the image analysis, we excluded calibration sources at the corners of the CCD chips. The images of the NXB were obtained from the night Earth data using XISNXBGEN (Tawa et al. 2008). Since the exposure times for the original data were different from that of the NXB, we calculated the appropriate exposure-corrected original and NXB maps using XISEXPMPGEN (Ishisaki et al. 2007). The corrected NXB images were next subtracted from the corrected original images. In addition, we simulated flat sky images using XISSIM (Ishisaki et al. 2007) and applied a vignetting correction. All the images obtained with XIS0 and XIS3 were combined. Throughout the reduction process, we also performed vignetting correction for all the XIS images described in Section 3. Finally, the images were smoothed with a Gaussian function with $\sigma = 0.07'$ (Gaussian kernel radius set as 8 in DS9).

With the combined XIS0+3 images, we first ran the source detection algorithm in XIMAGE to discriminate compact X-ray features from intrinsically diffuse X-ray emission. This is a well established approach as described in Giommi et al. (1992) and detailed in NASA’s HEASARC Software page¹¹. A few spots were seen only in the 0.4 – 2 keV or 2–10 keV

bands, but these were faint sources marginally detected below the 5σ level. The list and derived spectra of the bright compact emitters thus detected (all at approximately $\geq 5\sigma$), which are not associated with catalogued sources, are summarized in Appendix A.

For the spectral analysis, we used all the FI and BI CCDs, namely, XIS0, 1, 3 to maximize the photon statistics. For the bright compact X-ray features described above, we set the source regions to within $1' - 2'$ circles centered on the emission peaks, and estimated the backgrounds from annuli on the corresponding CCD chips with inner and outer radii of $2'$ and $4'$, respectively. The response (RMF) and auxiliary (ARF) files were produced using the analysis tools XISRMFGEN and XISSIMARFGEN (Ishisaki et al. 2007), which are included in the software package HEASoft version 6.12. For the analysis of the diffuse emission, we considered the en-

posed of three steps. First, using the BACKGROUND command, we estimated the background by dividing an image into equal boxes characterized by the typical PSF size, and rejecting those not complying with certain statistical criteria. The average in the remaining boxes was taken as the background value. Second, with the EXCESS command, a sliding-cell method was used to find areas with excesses over the background threshold (typically, $>3-5\sigma$). Finally, in the third step performed with the SEARCH command, we merged the excess cells into source boxes using the *Suzaku* PSF and vignetting to estimate source significances and statistics. Here we set the box sizes as $1.1' \times 1.1'$ (corresponding to 64×64 pixels) or $0.5' \times 0.5'$ (corresponding to 32×32 pixels) for crowded fields because of the blurring due to the *Suzaku* XIS PSF, and the detection threshold at 3σ . We performed the source detection separately in the 0.4 – 10 keV, 0.4 – 2 keV, and 2–10 keV ranges, and concatenated the results.

¹¹ <https://heasarc.gsfc.nasa.gov/docs/xanadu/ximage/examples/srcdet.html>. See also <https://heasarc.gsfc.nasa.gov/docs/xanadu/ximage/examples/backgd.html> for background calculation examples. In summary, the process was com-

ture CCD chip as a source region, but only after removing all the compact features detected above the 3σ level, with typical $2'$ radius circles (see Appendix A and Tables 3 & 4). The ARF files were produced assuming that the diffuse emission is distributed uniformly within circular regions with $20'$ radii (giving the ARF area of 0.35 deg^2) using XISSIMARFGEN and new contamination files (released on July 11, 2012). In contrast to the point source analysis, we did *not* subtract background photons from the region in the same CCD chip but instead modeled the isotropic background continuum (see Section 3.2.2 for details).

We note that even though the most recent version of XISSIMARFGEN reproduces well the degradation of the CCD quantum efficiency below 2 keV due to contamination¹², significant differences in the spectral shape of the measured emission continua between XIS 0, 1, and 3 were found below $\simeq 0.5$ keV. Therefore we did not use the spectral data below 0.6 keV for XIS 0 and 3, and below 0.4 keV for XIS 1. We also did not use the high energy data above 8 keV for XIS 1 due to low photon statistics. Light curves were also constructed for bright X-ray compact features, none of which indicated any significant variability within the short exposures performed.

3. RESULTS

3.1. X-ray Images

The obtained 0.4 – 10 keV XIS images (combined XIS 0 and 3) are shown in Figure 2 for the north-east field (N1–N8; from *top-left* to *bottom-right*), and in Figure 3 for the southern field (S1–S6; from *top-left* to *bottom-right*). At first glance, one can note some difference between the different pointings in the north, such that the surface brightness of the targeted regions gradually decreases across the bubble’s edge toward the GC from the outermost (N1) to the innermost (N8) pointings. On the other hand, this trend is not as clear in the south (from S1 to S6). In the figures, magenta crosses mark the positions of compact X-ray features detected at $\gtrsim 5\sigma$ level which are likely associated with catalogued background sources from the NED or SIMBAD database. The other X-ray features detected with *Suzaku* at high significances, which are missing any obvious Galactic or extragalactic identifications, are denoted as “src1-11” in the north, and “src1-10” in the south. A few bright features seen in the images but not listed here are spurious sources arising from instrumental artifacts (e.g., near the corners of the CCD chips). Red circles or ellipses in Figures 2 and 3 indicate the source extraction regions for the *unassociated* compact X-ray emitters.

With the given photon statistics and the relatively large PSF of the XIS, it is impossible to determine if the detected compact features are point-like, or if they are (marginally) extended. In this context, it is important to estimate the number of background AGN likely to be found within each XIS field of view (FOV). Following Stawarz et al. (2013), who utilized the results of the *Chandra* Deep Field-South observations (Tozzi et al. 2001), one should expect the number of AGN with 0.5 – 2 keV or 2 – 10 keV fluxes $> 5 \times 10^{-14} \text{ erg cm}^{-2} \text{ s}^{-1}$ to be $\sim 40/\text{deg}^2$ at most. This implies two or three uncatalogued AGN within each XIS FoV, which is close to the number of detected compact X-ray features without any obvious optical identification. In order to elaborate more on the possible AGN associations, we have investigated the available mid-infrared (MIR) maps of the areas

covered by our *Suzaku* exposures using the NASA Widefield Infrared Survey Explorer (*WISE*; Wright et al. 2010) satellite data. The all-sky *WISE* data release was searched for sources present within radii of $1.5''$ around the positions of the region centers listed in the Appendix A and no infrared counterparts were found.

3.2. X-ray Spectra

3.2.1. Compact X-ray Features

We first fitted the spectra of all the unassociated compact X-ray features detected at significance levels above $\gtrsim 5\sigma$ using XSPEC (see Table 5). Within the given photon statistics, the X-ray spectra were all well represented by single power-law models moderated by the Galactic absorption, with the exception of src2 in the N1 field which required a substantial excess absorption in the neutral hydrogen column density $N_{\text{H}} = 6.9_{-3.4}^{+6.2} \times 10^{22} \text{ cm}^{-2}$ with respect to the Galactic value of $N_{\text{H,Gal}} = 3.37 \times 10^{20} \text{ cm}^{-2}$. While the nature of this source is unclear, considering only one such source detected in all the *Suzaku* fields, it could be a background type-II AGN where the soft X-ray emission is heavily obscured by thick surrounding material (e.g., Krumpe et al. 2008). The results of the spectral fitting for these uncatalogued X-ray emitters are tabulated in Appendix A. Because of the large spread in their fitted spectral parameters – unabsorbed 2–10 keV fluxes with a range $(0.1 - 7.5) \times 10^{-13} \text{ erg cm}^{-2} \text{ s}^{-1}$ and photon spectral indices Γ ranging from 0.8 to 3.1 – it is difficult to draw robust conclusions on the nature of the compact X-ray sources. Nevertheless, the number density of the detected X-ray spots (two at most per individual XIS FoV) is comparable to that expected for background AGN as noted above (Section 3.1). Moreover, there is no systematic difference in the number of point-like sources detected in different fields at different distances from the GC. This again suggests that the compact X-ray features are most likely unrelated to the diffuse GH/NPS structure, but are rather background objects.

3.2.2. Diffuse Emission

As detailed in Section 2.2, we considered the entire CCD chip as a source region for the analysis of the diffuse emission after removing all the compact features detected above 3σ significances, regardless of whether they were catalogued or uncatalogued X-ray sources (see Appendix A and Tables 3 & 4). The spectra of the *Suzaku* pointings were all fitted with a three component model APEC1 + WABS*(APEC2 + PL). The model includes an *unabsorbed* thermal component (denoted as APEC1) representing the Local Bubble (LB) emission and/or contamination from the Solar-Wind Charge Exchange (SWCX; Fujimoto et al. 2007), an *absorbed* thermal component (denoted as APEC2) representing the GH or NPS, and an *absorbed* power-law component (denoted as PL) corresponding to the isotropic CXB radiation. As for the absorbed diffuse emission, the neutral hydrogen column density was fixed to the Galactic value $N_{\text{H,Gal}}$, in the direction of each pointing (see Table 2), while the photon index for the CXB component was fixed at $\Gamma_{\text{CXB}} = 1.41$ (Kushino et al. 2002). In the cases where N_{H} was left free in the spectral fitting, we also list the ratio of the absorbing column density to the full Galactic column, $N_{\text{H}}/N_{\text{H,Gal}}$ (Table 2). Note that within the statistical errors, most of the values are either consistent with unity, or even larger than unity (for N2, N5 and N7). However, due to the relatively low photon statistics in the southern pointings, we can provide only upper limits hence the re-

¹² <http://heasarc.gsfc.nasa.gov/docs/astroe/propTools/suzaku/simmarfgen.html>

TABLE 2
FITTING PARAMETERS FOR THE DIFFUSE EMISSION COMPONENT

ID	$N_{\text{H,Gal}}^a$ (10^{20} cm $^{-2}$)	$N_{\text{H}}/N_{\text{H,Gal}}^b$	kT_1^c (keV)	EM_1^d (10^{-2} cm $^{-6}$ pc)	kT_2^e (keV)	EM_2^f (10^{-2} cm $^{-6}$ pc)	CXB Norm g	χ^2/dof
North Bubble								
N1	3.37	0.8-3.8	0.1(fix)	3.47 ± 0.38	$0.299^{+0.012}_{-0.010}$	5.49 ± 0.38	$1.14^{+0.04}_{-0.03}$	1.07/144
N2	3.83	2.9-5.5	0.1(fix)	3.26 ± 0.45	$0.315^{+0.011}_{-0.012}$	5.38 ± 0.36	1.03 ± 0.03	1.38/162
N3	3.86	0.8-4.1	0.1(fix)	4.09 ± 0.71	$0.319^{+0.018}_{-0.015}$	5.28 ± 0.50	1.08 ± 0.05	1.07/96
N4	4.06	0.8-2.9	0.1(fix)	4.58 ± 0.49	$0.324^{+0.014}_{-0.012}$	5.11 ± 0.37	0.71 ± 0.04	1.35/135
N5	4.26	1.1-4.8	0.1(fix)	3.16 ± 0.44	$0.285^{+0.010}_{-0.009}$	5.40 ± 0.36	0.94 ± 0.03	1.19/148
N6	4.45	0.6-4.0	0.1(fix)	4.66 ± 0.43	$0.316^{+0.015}_{-0.013}$	3.82 ± 0.31	1.08 ± 0.03	1.20/166
N7	4.76	4.4-6.7	0.1(fix)	3.83 ± 0.40	$0.290^{+0.011}_{-0.010}$	4.56 ± 0.32	0.64 ± 0.03	1.25/153
N8	5.02	1.0-5.1	0.1(fix)	4.43 ± 0.53	$0.315^{+0.022}_{-0.018}$	3.28 ± 0.38	0.78 ± 0.03	1.08/106
South Bubble								
S1	1.84	< 1.8	0.1(fix)	$3.01^{+0.50}_{-0.64}$	$0.283^{+0.063}_{-0.049}$	$0.93^{+0.49}_{-0.28}$	1.02 ± 0.05	1.03/88
S2	1.66	< 2.6	0.1(fix)	$3.03^{+0.56}_{-0.55}$	$0.369^{+0.161}_{-0.064}$	$0.80^{+0.46}_{-0.28}$	$0.97^{+0.02}_{-0.04}$	1.15/71
S3	1.89	< 4.1	0.1(fix)	1.97 ± 0.63	$0.270^{+0.077}_{-0.039}$	$1.48^{+0.65}_{-0.50}$	$1.02^{+0.04}_{-0.05}$	1.49/62
S4	2.16	< 2.6	0.1(fix)	$2.59^{+0.51}_{-0.60}$	$0.260^{+0.045}_{-0.033}$	$1.37^{+0.55}_{-0.37}$	1.11 ± 0.04	1.15/100
S5	2.45	< 0.9	0.1(fix)	$3.03^{+0.42}_{-0.52}$	$0.262^{+0.043}_{-0.036}$	$1.15^{+0.50}_{-0.30}$	0.92 ± 0.03	1.22/117
S6	3.03	< 4.4	0.1(fix)	$4.06^{+0.65}_{-0.71}$	$0.325^{+0.104}_{-0.051}$	$1.18^{+0.42}_{-0.39}$	0.79 ± 0.05	1.22/117

NOTE. — ^a: The absorption column densities for the CXB and the GH/NPS components (WABS*(APEC2 + PL)) components were fixed to Galactic values given in Dickey & Lockman (1990).

^b: The ratio of the absorbing column density to the full Galactic column along the line of sight when N_{H} was left free in the spectral fitting.

^c: Temperature of the LB/SWCX plasma fitted with the APEC model for the fixed abundance $Z = Z_{\odot}$.

^d: Emission measure of the LB/SWCX plasma fitted with the APEC model for the fixed abundance $Z = Z_{\odot}$.

^e: Temperature of the GH/NPS plasma fitted with the APEC model for the fixed abundance $Z = 0.2 Z_{\odot}$.

^f: Emission measure of the GH/NPS plasma fitted with the APEC model for the fixed abundance $Z = 0.2 Z_{\odot}$.

^g: The normalization of the CXB in units of 5.85×10^{-8} erg cm $^{-2}$ s $^{-1}$ sr $^{-1}$, given in Kushino et al. (2002) as an average of 91 observation fields, assuming a power-law model with a photon index $\Gamma_{\text{CXB}} = 1.41$.

sults are not conclusively close to either zero or unity. Since the temperature and abundance of the LB plasma is still only poorly known, we fixed them at $kT = 0.1$ keV and $Z = Z_{\odot}$, respectively, which is a common approach in the literature (Willingale et al. 2003; Miller et al. 2008; Yao & Wang 2005; Yao et al. 2009, 2010). We note that the presence of the $kT \simeq 0.1$ keV component related to SWCX/LB is confirmed by the uniform analysis of 12 and 26 fields observed with *Suzaku* and *XMM*, respectively (Yoshino et al. 2009; Henley et al. 2010; Henley & Shelton 2013). The results of our spectral fitting are shown in Figures 4 & 5 and are summarized in Table 2.

All the diffuse X-ray spectra derived for the targeted fields were well represented by the adopted three-component model. Below 2 keV, the measured continua are dominated by the $kT \simeq 0.3$ keV thin thermal component (APEC2), although the $kT \simeq 0.1$ keV emission (APEC1) is still important, especially below 0.7 keV, to account for the OVII (574 eV) emission (the reduced χ^2 becomes unacceptable if we ignore the 0.1 keV component attributed to LB/SWCX). Even though each individual spectral fit cannot precisely constrain the abundance of the $kT \simeq 0.3$ keV component, we found that a sub-Solar metallicity (median $Z \simeq 0.2 Z_{\odot}$) is on average preferred (see Appendix B). The depleted abundance of $Z < 0.5 Z_{\odot}$ is also consistent with the previously reported NPS observations with *Suzaku* and *XMM* (Willingale et al. 2003; Miller et al. 2008). Meanwhile, we do not clearly see the enhanced Nitrogen abundance reported in Miller et al. (2008) possibly due to the fact that both the N1–8 and S1–6 regions are much fainter than those observed in the literature and to our shorter exposures. Hence, hereafter we fix the metallicity of the $kT \simeq 0.3$ keV component at $Z = 0.2 Z_{\odot}$. Also note that $N_{\text{H}}/N_{\text{H,Gal}}$ is generally large, exceeding unity for some of

the north-east pointings, suggesting the presence of a large amount of neutral matter absorbing the X-ray emission of the structure.

Above 2 keV, the X-ray spectra are dominated by the contribution of the PL component in all the fields (N1–N8, S1–S6). Assuming this emission is isotropic, the 2–10 keV unabsorbed PL intensity is basically consistent with the absolute intensity of the CXB, namely $(5.85 \pm 0.38) \times 10^{-8}$ erg cm $^{-2}$ s $^{-1}$ sr $^{-1}$ (Kushino et al. 2002). We do see some “pointing-to-pointing” intensity variations within the range $(3.8 - 6.7) \times 10^{-8}$ erg cm $^{-2}$ s $^{-1}$ sr $^{-1}$, meaning $(0.64 - 1.14) \times$ the average CXB level (Table 2), but this level of uncertainty is naturally expected from the large-scale fluctuation of the CXB itself as concluded in Kushino et al. (2002) and also demonstrated by Yoshino et al. (2009). This indicates that we do *not* see any excess non-thermal PL emission associated with the Fermi Bubbles, at least at the level well exceeding fluctuation of the CXB intensity. To derive an upper limit for the non-thermal emission from the bubbles, we reanalyzed the X-ray spectra of the expected inner bubble regions (i.e., N7–8 and S2–6) by adding an additional PL component (with fixed photon index, $\Gamma = 2.0$) to the one contributed by the CXB. The obtained 90% confidence level upper limit for the unabsorbed 2–10 keV PL emission associated with the Fermi Bubble is $< 9.3 \times 10^{-9}$ erg cm $^{-2}$ s $^{-1}$ sr $^{-1}$, which corresponds to $\sim 15\%$ of the CXB intensity. We revisit this issue below (Section 4.3) when modeling the overall SED of the Fermi Bubbles from radio to GeV γ -rays.

Finally, in Figure 6 we plot the changes in the APEC2 spectral fitting parameters, namely the emission measure (EM) and plasma temperature kT , for the north-east (N1–N8) and the southern (S1–S6) fields, as a function of a separation an-

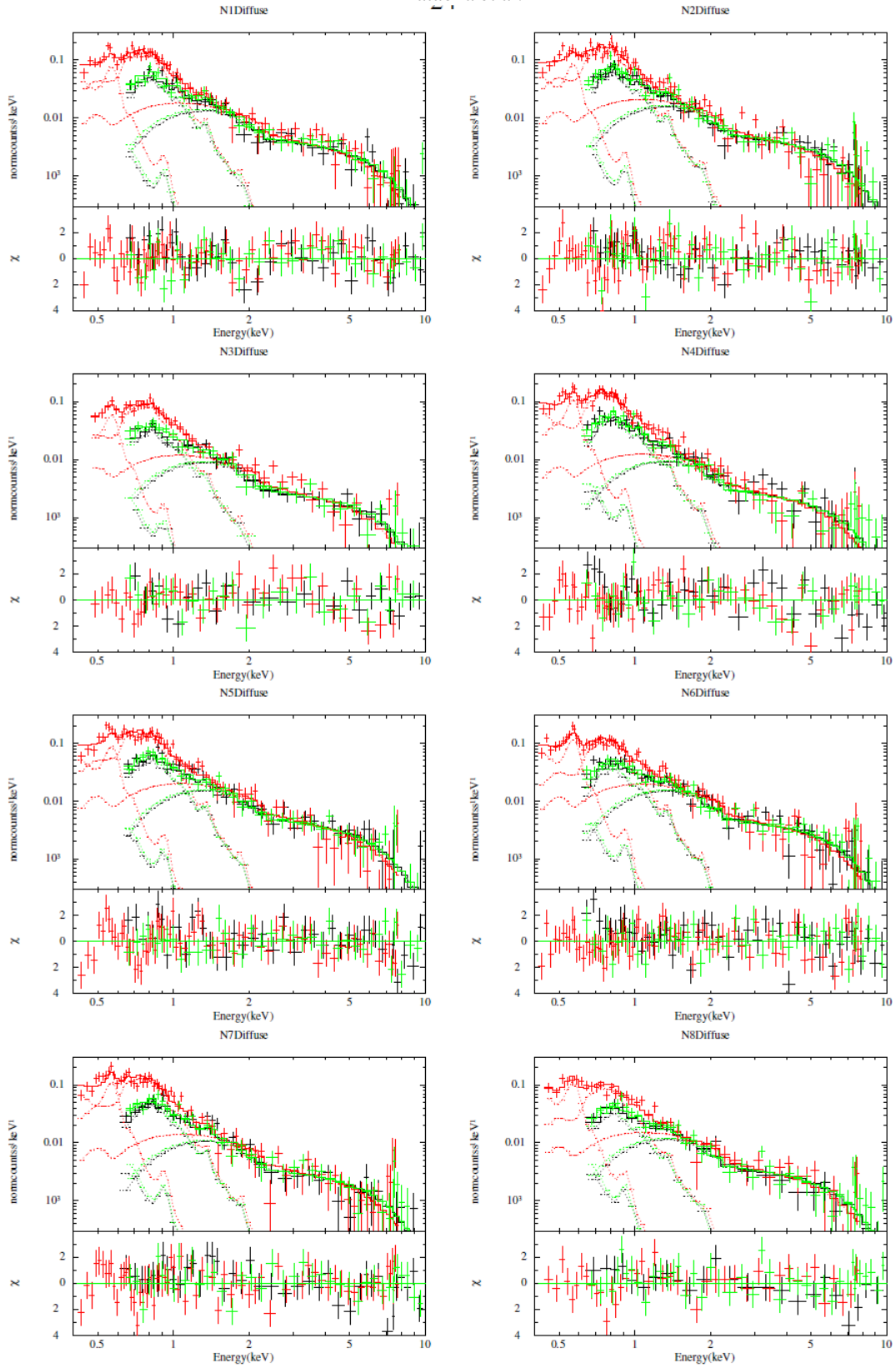


FIG. 4.— The XIS spectra of the diffuse emission component for the N1–N8 pointings, together with the best fit model curves (APEC1+WABS*(APEC2+PL)) and residuals. The LB component ($kT \simeq 0.1$ keV; APEC1) dominates the lowest 0.4–0.6 keV range, thermal emission related to the NPS and/or Galactic halo ($kT \simeq 0.3$ keV; APEC2) dominates the 0.6–1.5 keV range, and a power-law component from the CXB dominates above 1.5 keV ($\Gamma \simeq 1.4$; PL). XIS 0 data/fits are shown in black, XIS 1 in red, and XIS 3 in green.

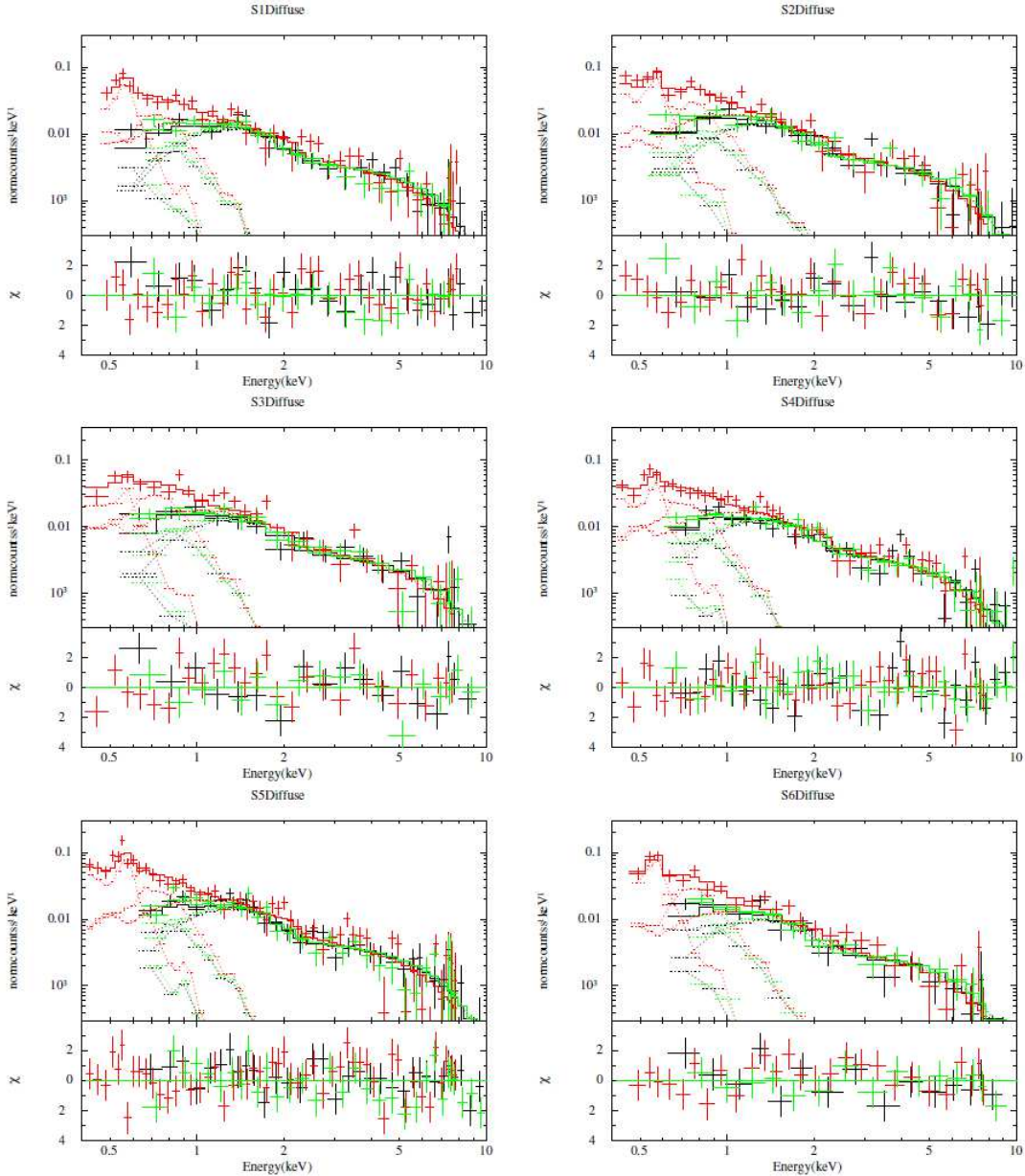


FIG. 5.— As in figure 4, but for the S1–S6 pointings.

gle from the expected boundary of the bubble’s edge (following Su et al. 2010). Interestingly, the EM of the $kT \simeq 0.3$ keV component appears to change significantly and abruptly (by about $\simeq 50\%$) around the north-east edge (i.e., between pointings N6 and N7). The constant fit to the EM profile resulted in a χ^2 value of 37.6 for 7 degree of freedom with a corresponding probability, $P(\chi^2) < 10^{-5}$. Note the probability increased significantly to $P(\chi^2) = 0.96$ if we fit the EM between N1 and N5 only ($\chi^2 = 0.61$ for 4 degrees of freedom). This change is not due to any artifact in the spectral fitting, e.g., an increased amount of contamination from the LB/SWXC component as we checked in careful detail (Appendix C), although there still remains a possibility that we are seeing local X-ray features such as clumps or filaments *within* the NPS rather than an EM change physically associated with the north-east bubble edge. The analogous “jump” in the EM is not as clear in the southern bubble edge, and this

could be partly explained in this case because we have only one FOV (S1) just outside the edge. But as we argue below (Section 4.1), since the *ROSAT* 0.75 keV map can be considered as a good tracer of the GH/NPS component, the absence of any NPS-like feature south from the GC may suggest that no sharp boundary is present there. Also note that the temperature of the APEC2 component is almost constant in both the north-east and southern fields. This temperature is a bit higher than the canonical value of the GH, $kT \simeq 0.2$ keV, derived for Galactic longitudes $65^\circ < l < 295^\circ$ (Yoshino et al. 2009) or $120^\circ < l < 240^\circ$ (Henley et al. 2010) to avoid contamination from the GC region. Very recent measurements of the Galactic halo’s X-ray emission using 110 *XMM* observations also confirm its temperature is fairly uniform (median = 0.19 keV, interquartile range = 0.05 keV; Henley & Shelton 2013).

4. DISCUSSION

4.1. Comparison with RASS Maps

In section 3.2.2, we showed that the diffuse X-ray emission, after removing compact X-ray sources and features detected at $\geq 3\sigma$ level, is generally well reproduced by the three component plasma model: (1) $kT \simeq 0.1$ keV emission due to the LB with some contamination from SWCX, (2) $kT \simeq 0.3$ keV plasma related to the GH and/or NPS gas, and (3) $\Gamma \simeq 1.4$ power-law as expected from the CXB. Particularly noteworthy is that the EM of the GH/NPS component gradually drops by $\simeq 50\%$ around the expected boundary of the north-east Fermi Bubble edge. This drop is consistent with a visual impression from both *ROSAT* all sky survey *R45* (0.75 keV) and *R67* (1.5 keV) maps, indicating that the X-ray surface intensity gradually decreases from the N1 to N8 fields (see, Fig. 1 *top-left*), away from the NPS. However, the *ROSAT* maps alone are not sufficient to quantify the observed changes in the plasma parameters, simply because here we are dealing with a multi-temperature convolution of various emission components and *ROSAT* images do not provide the necessary detailed spectral information.

In order to investigate this issue in more detail, in Figure 7 (*top panel*) we present the observed *ROSAT* (*R45*) counting rate at 0.75 keV, as a function of the EM (for the APEC2 component strictly), which we obtained from the N1–N8 and S1–S6 pointings, along with the EM values of the GH/NPS components measured at the NPS center at low Galactic latitudes in the previously reported *Suzaku* and *XMM* observations (see Figure 1; Willingale et al. 2003; Miller et al. 2008). The horizontal error bars in the figure correspond to 1σ statistical errors for the EM values estimated from the spectral model fits of the *Suzaku* (or *XMM*) data (see Table 2), while the minimum and maximum counting rates in the *ROSAT* map (Snowden et al. 1995, 1997) are given to indicate approximately the fluctuations present in the *ROSAT* data centered on the same observing region (e.g., Yoshino et al. 2009). Considering the angular resolution $\sim 0.2^\circ$ of the *ROSAT* maps (Snowden et al. 1997), we estimated the source counts within circles with radius $\sim 0.2^\circ$. Here we do not exclude contributions from point features in the *ROSAT* maps because no bright X-ray sources were in the regions of interest. In fact, we confirmed that the sum of the X-ray fluxes from the compact X-ray features detected by *Suzaku* (Section 3.2.1) constitute less than 5% of the diffuse emission in the 0.5–2 keV energy range. Also the contribution of unresolved sources in the 1–2 keV band measured by *ROSAT* is 4.4×10^{-12} erg s^{-1} cm^{-2} deg^{-2} (Hasinger et al. 1998; Tozzi et al. 2001), which again corresponds to $\simeq 5\%$ of the diffuse emission in the 0.5–2 keV energy range. However, we remark that even sources situated well outside the *Suzaku* field of view ($17' \times 17'$) may contribute significantly to the reported *ROSAT* counting rates, hence contamination from background sources may be more significant than approximated above. Figure 7 (*bottom panel*) presents the analogous counting rates measured at 1.5 keV (*R67* band).

As shown in Figure 7, the *R45* counting rates appear overall to track the EM of the GH/NPS component surprisingly well with a correlation factor 0.97 ± 0.01 . However, inspecting the data from the *Suzaku* pointings of the north-east (N1–8) and south (S1–6) regions in more detail suggests the correlation does not hold well within these observations. This could be due to local (but small) variations in the thermal plasma parameters (e.g., abundance; see Appendix C), differ-

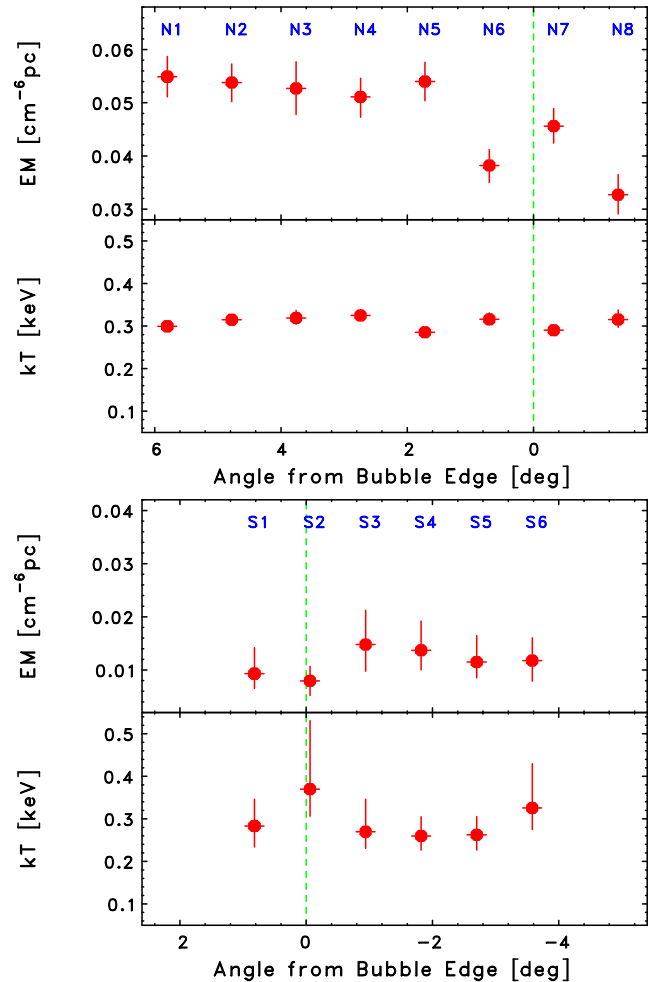


FIG. 6.— Variation in the spectral fitting parameters EM and kT for the APEC2 emission component in the north-east (*top*) and south (*bottom*) bubble *Suzaku* observations, as a function of the angular separation from the bubble edge. Note a significant decrease of the EM around the expected position of the bubbles' boundary (green dotted line following Su et al. 2010) in the north, with no accompanying changes in the plasma temperature.

ing contributions from the contaminating sources especially in the *ROSAT* maps, and fluctuations of the CXB intensity (although this spectral component contributes negligibly to the *R45* bandpass). The contribution and superposition of such background sources is predominantly negligible for the previous NPS pointings because they pointed at much brighter parts of the NPS at low Galactic latitude. Even with such complications, it appears the *R45* map data can still serve as a useful overall tracer of the distribution of the GH gas even though the *ROSAT* maps carry no explicit spectral information. In contrast, in the *R67* map (1.5 keV) the contribution from the CXB becomes significant, diluting any intrinsic correlation between the 1.5 keV counting rate and the EM of the GH/NPS component (correlation factor reduced to 0.86 ± 0.02). In this band, additional fluctuations in the *ROSAT* counting rates above 1 keV could be expected due to an increased amount of background sources like AGN due to the poorer resolution of these data with respect to that of *Suzaku*.

The correlation between the *ROSAT* *R45* counting rate and the $kT \simeq 0.3$ keV plasma EM derived from the *Suzaku* observations may suggest that the X-ray spectra around the north-

east and southern Fermi Bubbles resemble each other, even though the giant NPS structure is seen only in the north. Indeed, what we found is that the diffuse X-ray emission around the bubbles both above and below the GC, is well characterized by the three-component model introduced above, with similar values of the fitted model parameters. The same holds for the previously X-ray targeted fields of the bright center of the NPS analyzed in Willingale et al. (2003) and Miller et al. (2008). Note that in these previous works, the GH emission was assumed to be composed of an *absorbed* $kT \simeq 0.1$ keV component superimposed on the $kT \simeq 0.26$ keV continuum attributed to the NPS, and distinct from the GH emission. Although this observational fact could be a chance coincidence and we cannot rule out the possibility that all the emission is simply from the local structure, it appears as likely that the $kT \lesssim 0.3$ keV temperature gas seen at the position of the Fermi Bubbles, including the NPS structure, is of the same GH origin.

4.2. NPS: Shock-Heated Galactic Halo Gas?

Previously, it was widely agreed that the NPS and the rest of the Loop I structure arises from a recent supernova shock wave heating the outer shell of the superbubble, at a distance of about 100 pc from the Sun (Berkhuijsen et al. 1971; Egger & Aschenbach 1995). Only recently, after the discovery of the Fermi Bubbles in particular, has the alternative interpretation stating that the NPS is a remnant of a starburst or a nuclear outburst which happened near/within the GC about 15 Myr ago (Sofue 1977, 1984, 1994, 2000, 2003; Bland-Hawthorn & Cohen 2003) entered back into the limelight. The argument against the GC scenario followed from the measurement of the interstellar polarization at a distance of about 100 pc, which seems to trace some part of Loop I including the NPS (Bingham 1967; Mathewson & Ford 1970). However, the observed stellar polarization orientation is almost *perpendicular* to the direction of the NPS, especially at low Galactic latitudes, which is at odds with the SNR association (e.g., Furst & Reich 1990; Xu et al. 2007; Xiao et al. 2008). Specifically, the NPS radio ridge at $b = 20\text{--}30^\circ$ runs at angle 130° (from GC toward $l = 90^\circ$; Sofue & Reich 1979), while the optical polarization is at $40\text{--}60^\circ$ (Mathewson & Ford 1970). Thus, the implied local magnetic field orientation is nearly perpendicular to the NPS and does not support the local SNR origin. It has also been argued that the observed optical polarization is aligned with HI filaments of the Hydra ridge, which is a local HI region inflated by magnetic fields, and unrelated to non-thermal features like the NPS (Sofue 1973, 1976). The Hydra HI ridge at $b = 20\text{--}30^\circ$ also runs at $20\text{--}50^\circ$, nearly perpendicular to the NPS. Note that HI at $b = 70\text{--}90^\circ$ appears parallel to the NPS orientation, and that has been taken as evidence for the HI–NPS association. However, as mentioned above, the brightest part of the NPS at $b = 20\text{--}30^\circ$ is perpendicular to HI. For further details of these arguments, see the discussion in Sofue et al. (1974).

One should note further that both the *Suzaku* and *XMM* observations targeting any part of the NPS implied relatively large values of the neutral hydrogen column density N_{H} absorbing the NPS thermal spectrum in all cases. For example, based on the *XMM* data, Willingale et al. (2003) derived column densities 0.9, 0.6, and 0.5 times the Galactic value $N_{\text{H, Gal}}$, for the three different regions positioned at $(l, b) = (25.0^\circ, 20.0^\circ)$, $(20.0^\circ, 30.0^\circ)$, $(20.0^\circ, 40.0^\circ)$, respectively (see Figure 1 for the *XMM* pointing positions). Similarly,

Miller et al. (2008) concluded from spectral fitting of *Suzaku* data on the brightest part of the NPS, $(l, b) = (26.84^\circ, 21.96^\circ)$, was either > 0.71 or > 0.97 times the Galactic value, depending on the choice of background regions. At first glance, such high levels of N_{H} (i.e., column densities more than 0.5 times the *total* Galactic value toward in the line-of-sight direction), confirmed by our analysis of the newly acquired *Suzaku* data, seems to conflict with the idea that the NPS is a local phenomenon. Willingale et al. (2003) mention that the halo and NPS components lie behind at least 50% of the line-of-sight cold gas for which the total Galactic column density in the range $(2\text{--}8) \times 10^{20} \text{ cm}^{-2}$, and attribute this high N_{H} to the cold gas distribution in the wall located at 15–60 pc. However, the presence of such a wall between the LB and NPS is not confirmed, but was rather an assumption made in order to not conflict with their local model. Miller et al. (2008) also reported high levels of N_{H} but no discussion about the origin of such large amount of cold gas; throughout, they assumed that the NPS is a local structure based on the interstellar polarization feature and the HI features, both of which cannot however be taken to strongly support the local interpretation as we discuss above.

Moreover, the inspection of the *ROSAT* maps indicates that the X-ray emission from the NPS is heavily absorbed at 1.5 keV at low Galactic latitudes (e.g., Snowden et al. 1995), i.e., from the Galactic plane up to $b \simeq 10^\circ$. This requires hydrogen column densities as large as $\gtrsim 5 \times 10^{21} \text{ cm}^{-2}$. Meanwhile, any accumulation of neutral gas within a 100 pc distance by an expanding shock wave should amount to no more than $N_{\text{H}} \simeq 3 \times 10^{20} \text{ cm}^{-2}$. Therefore, it seems reasonable and natural to consider the $kT \simeq 0.3$ keV plasma component detected in our *Suzaku* observations of the north-east and southern Fermi Bubbles' edges is essentially the same as the plasma component seen in the previous observations of the NPS, having the similar temperature, $kT \simeq 0.3$ keV. Yet it is difficult to conclude if the NPS is physically associated with the GH, because as already emphasized above, the derived temperature of this component is slightly higher than the “canonical” $kT \simeq 0.2$ keV value claimed for the GH gas (Yao & Wang 2005; Yao et al. 2009, 2010; Yoshino et al. 2009; Henley et al. 2010; Henley & Shelton 2013). On the other hand, this discrepancy can be explained as a signature of gas heating by the expanding bubble structure, which drives a low-Mach number shock in the surrounding medium (for a high-Mach number case see, Guo & Mathews 2012; Guo et al. 2012). We return to this issue in Sections 4.3 and 4.4.

Finally, let us comment in this context on the aforementioned jump in the EM of the hot gas component at the north-east bubble edge. Here we propose that the observed 50% decrease in EM is likely due to projection effects related to a cavity inflated by an expanding bubble in the GH environment. Namely, assuming that the Fermi Bubbles are indeed characterized by sharp edges and are symmetric with respect to the observer's line of sight, a shell of the evacuated gas is expected to form an envelope around the expanding structure. A projection of the emission of this shell onto the bubbles' interior should then result in the same temperature plasma component (here $kT \simeq 0.3$ keV) being observed from both within and around the bubbles even if they are devoid of any thermal component, but only with the enhanced emissivity just outside the bubbles' edges. To estimate the exact shape of the EM profile requires detailed modeling of the emissivity profile as proposed to model the radial profile of shell-type supernova remnants (e.g., Berezhko & Völk 2004),

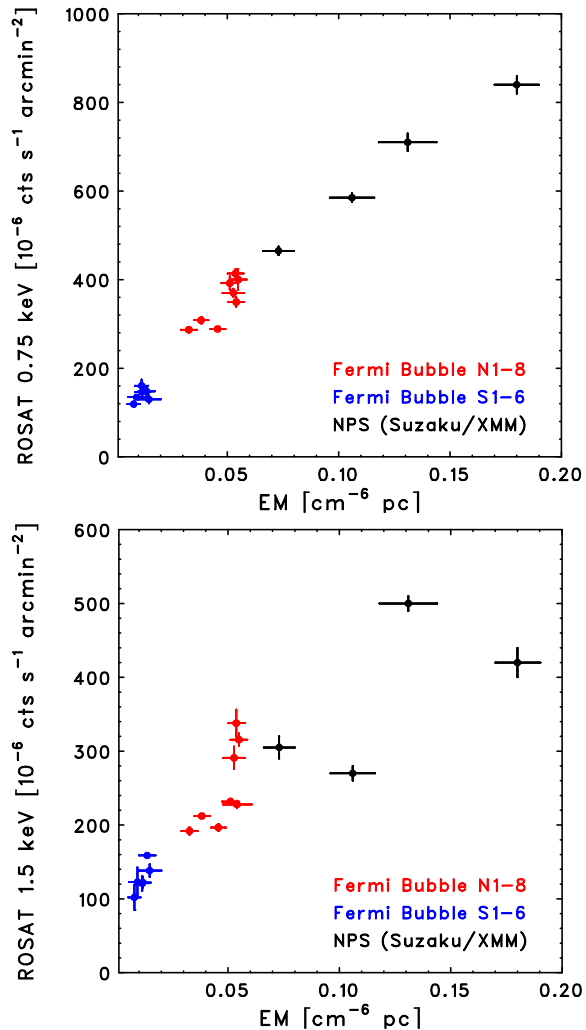


FIG. 7.— *ROSAT* count rates in units of 10^{-6} cts s^{-1} , taken from the 0.75 keV (*top*) and 1.5 keV (*bottom*) maps, compared with our *Suzaku* estimates of the EM for the GH/NPS component. Included also are the archival *Suzaku* or *XMM* observations of the NPS (Willingale et al. 2003; Miller et al. 2008).

which is beyond the scope of this paper. Instead, we consider a simple 2-dimensional toy model in which the uniform gas is confined in a donut region between R_{in} and R_{out} , where $R_{\text{in}} \simeq 4$ kpc is the radius of the bubble and the observed EM is simply proportional to the path length of gas along the line of sight. Within such a toy model, a 50% drop of EM can be explained if the width of the outer shell of the bubble, $R_{\text{out}} - R_{\text{in}} \simeq 2$ kpc, i.e., is twice smaller than the bubble radius.

4.3. Thermal vs Non-thermal Plasma

In the spectral fitting of the newly acquired *Suzaku* data, we did not detect any excess non-thermal emission associated with the bubbles, at least at the level exceeding the expected $\sim 10\%$ fluctuations in the CXB. Figure 8 shows the SED of the Fermi Bubbles, from radio to GeV γ -ray, with the corresponding X-ray upper limit. The GeV data points correspond to the emission of the entire bubbles' structure following Su et al. (2010). The radio data points corresponds to the WMAP haze emission averaged over $b = -20^\circ$ to -30° , for $|l| < 10^\circ$. The bow-tie centered on the 23 GHz

K-band indicates the range of synchrotron spectral indices allowed for the WMAP haze following Dobler & Finkbeiner (2008). In our modeling, we assumed a simple one-zone leptonic model in which the radio emission and GeV γ -ray emission arise from the same population of relativistic electrons through the synchrotron and inverse-Compton (IC/CMB) processes, respectively (e.g., Su et al. 2010). We are aware that detailed modeling requires also the IC contributions from the dust and starlight, i.e., far infrared and optical/UV backgrounds as detailed in Mertsch & Sarkar (2011). However, such starlight/dust emission at the position of the lobes is anisotropic and non-uniform, therefore special care must be taken when including these additional sources of seed photons. The interstellar stellar radiation field has energy density of ~ 1 eV cm^{-3} , comparable to that of the CMB, but its contribution is more significant closer to the disk and as such, the conclusion is not significantly affected at high galactic latitudes. In fact, Mertsch & Sarkar (2011, Fig. 2 therein) demonstrated that the IC/CMB contribution is most significant up to 10 GeV in the *Fermi*-LAT data.

For the electron energy distribution we assume a standard broken power-law form $N_e(\gamma > \gamma_{\text{min}}) = N_0 \gamma^{-s} \left(1 + \frac{\gamma}{\gamma_{\text{brk}}}\right)^{-1} \times \exp\left[-\frac{\gamma}{\gamma_{\text{max}}}\right]$, with the injection index $s = 2.2$, and the minimum and maximum electron Lorentz factors set to $\gamma_{\text{min}} = 2000$ and $\gamma_{\text{max}} = 10^8$, respectively. The parameter $\gamma_{\text{brk}} = 10^6$ is the characteristic energy above which the electron spectrum breaks by $\Delta s = 1$. We further anticipate the magnetic field intensity $B = 12 \mu\text{G}$ within the bubbles, and the emission volume $V = 2 \times \frac{4}{3}\pi R^3$ with radius $R = 1.2 \times 10^{22}$ cm. The modeling results, shown in Figure 8 as a blue curve, yield the non-thermal bubbles' pressure $p_{\text{n/th}} = (U_e + U_B)/3 \simeq 2.0 \times 10^{-12}$ dyn cm^{-2} , where the electron and magnetic field energy densities are $U_e = \int d\gamma m_e c^2 \gamma N_e(\gamma)$ and $U_B = B^2/8\pi$, and the total non-thermal energy stored in electrons and magnetic field $E_{\text{n/th}} = (U_e + U_B) \times V \simeq 10^{56}$ erg. The results of our model fitting suggest $U_B \gg U_e$. Note that the derived $B = 12 \mu\text{G}$ seems a factor of 2–4 higher than the typical magnetic field in our Galaxy, but consistent with independent estimates in the literature of $B = 15 \mu\text{G}$ (Mertsch & Sarkar 2011) or $B = 5 - 10 \mu\text{G}$ (Su et al. 2010). Following Mertsch & Sarkar (2011), this could be due to an overestimate of microwave flux caused by inappropriate template subtraction. In fact, the model prediction assuming $B = 4 \mu\text{G}$ suggests an order of magnitude smaller flux for the WMAP haze so more detailed modeling of the SED will be justified only after updated *Planck* and *Fermi*-LAT measurements are made available. Similarly at this stage, we can neither support or rule out various other models including the hadronic model we mentioned in the introduction section (Crocker & Aharonian 2011). Therefore, our IC/CMB model should be considered as one possible interpretation that should be clarified and tested in the near future.

For comparison, we can also estimate the thermal pressure of the NPS gas as $p_{\text{th}} \simeq n_g \times kT$, where n_g is the gas number density and kT is the gas temperature. From our *Suzaku* observations we take $kT \simeq 0.3$ keV, and estimate $n_g = (\text{EM}/d)^{1/2}$, where d is the scale length of the X-ray plasma with the given emission measure EM. Assuming the thickness of a thermal X-ray envelope/shell (see the discussion in Section 4.2) as $d \simeq 2$ kpc, we obtain $p_{\text{th}} \simeq 2 \times 10^{-12}$ dyn cm^{-2} and $E_{\text{th}} \simeq 10^{56}$ erg. Even though all

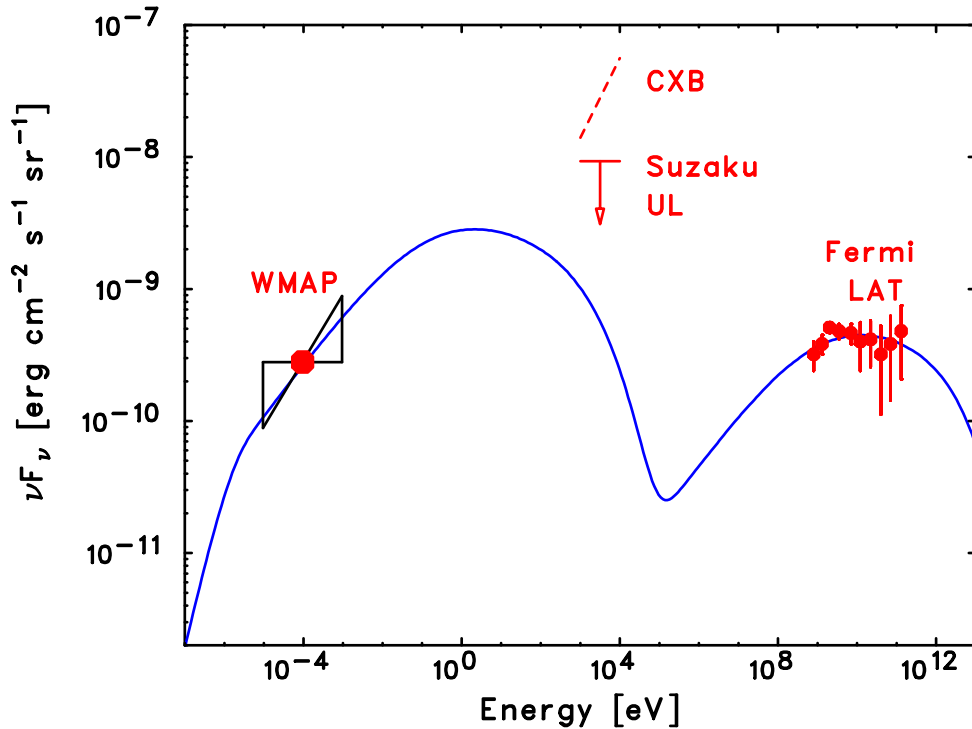


FIG. 8.— SED of the Fermi Bubbles fitted with the one-zone leptonic model (blue curve). We assumed the magnetic field intensity $B = 12 \mu\text{G}$ within the bubbles, and the emission volume $V = 2 \times \frac{4}{3}\pi R^3$ with radius $R = 1.2 \times 10^{22}$ cm. Full details are given in Section 4.3. The GeV data points correspond to the emission of the entire bubbles' structure, following Su et al. (2010). The radio data points corresponds to the WMAP haze emission averaged over $b = -20^\circ$ to -30° , for $|l| < 10^\circ$. The bow-tie centered on the 23 GHz K -band indicates the range of synchrotron spectral indices allowed for the WMAP haze, following Dobler & Finkbeiner (2008). Red dashed line denotes the observed CXB level, and the solid line indicates the *Suzaku* upper limit for the bubbles' non-thermal X-ray emission, $< 9.3 \times 10^{-9}$ erg cm $^{-2}$ s $^{-1}$ sr $^{-1}$ in the 2–10 keV energy range, corresponding to $\sim 15\%$ of the CXB level.

these estimates are rough, and are based on clearly oversimplified modeling, they indicate robustly that under all the model assumptions specified above, the non-thermal plasma filling the Fermi Bubbles and the thermal plasma of the bubbles' immediate surroundings are in pressure and energy equipartition. This finding is in accord with the idea that the NPS feature is composed of the GH gas heated by a shock wave driven by the expanding bubbles. Indeed, in such a situation, pressure equilibrium between shock downstream fluids is expected.

In the framework of the above interpretation, the Mach number of a shock following from the observed temperature ratio $kT_+/kT_- \simeq 0.3 \text{ keV}/0.2 \text{ keV}$ is $\mathcal{M} \simeq 1.5$, assuming the adiabatic parameter of the GH gas $\hat{\gamma} = 5/3$. This further implies the upstream (unperturbed GH gas) pressure $p_- \simeq 0.8 \times 10^{-12}$ dyn cm $^{-2}$, and the shock velocity $v_{\text{sh}} \simeq \mathcal{M} \times c_{s-} \simeq 320 \text{ km s}^{-1}$ for the upstream sound speed $c_{s-} \simeq 200 \text{ km s}^{-1}$. As discussed below, the estimated value of v_{sh} is in agreement with the expected expansion velocity of the Fermi Bubbles.

4.4. On the Formation of the Fermi Bubbles

Let us comment here on the formation of the Fermi Bubbles in the context of the presented *Suzaku* observations. Note again that the discussion below is our speculation based on an assumption that both the Fermi Bubbles and NPS are connected with the GC past activity. Therefore as we have shown above, the local bubble scenario for the NPS can also work in some sense and still leaves a lot of room to be clarified in future works. Nevertheless, there are a number of observations discussed in the literature taken as evidence that the

GC has undergone multiple past epochs of enhanced activity on different timescales, due either to AGN-like outbursts or episodes of circumnuclear starbursts. The strongest case among these is the Fe K_α echo from molecular clouds situated a few hundreds parsec apart around Sgr A* (Koyama et al. 1996; Murakami et al. 2000, 2001). Recently, a diffuse clump in an over-ionized state with a jet-like structure has also been found in the *Suzaku* data for the GC south, ~ 200 pc from Sgr A*, suggesting a plasma ejection from Sgr A* which happened about a million years ago (Nakashima et al. 2013, in prep). Outflows of this kind are expected to lead to the formation of bubbles/lobes expanding within the Galactic halo, just like the GC scenario of NPS as well as the Fermi Bubbles, sweeping up the interstellar/halo gas in analogy with the extended lobes seen in distant radio galaxies (Sofue 2000). Totani (2006) has shown that the Fe K_α echo, NPS, and the observed 511 keV line emission toward the GC can be explained naturally in a standard framework of a radiatively inefficient accretion flow (RIAF) in the GC black hole, if the typical accretion rate was about 1,000 times higher than the current rate in the past 10 Myr. The outflow energy expected by such an accretion rate is expected to be 10^{56} erg (or 3×10^{41} erg s $^{-1}$).

The GH is thought to be rather isothermal, characterized by a temperature, $kT \simeq 0.2 \text{ keV}$, with only some density gradients towards the GC (Yoshino et al. 2009; Henley et al. 2010; Henley & Shelton 2013). During the evolution of the outflow, the evacuated halo gas can be heated, if the bubbles' expansion is supersonic, due to formation of a shock wave at the edges of the structure. In the previous section we estimated the Mach number of a shock needed to heat the

GH gas from $kT \simeq 0.2$ keV up to $kT \simeq 0.3$ keV characterizing the NPS emission as $\mathcal{M} \simeq 1.5$, corresponding essentially to the trans-sonic expansion velocity of the Fermi Bubbles $v_{\text{exp}} \sim 300 \text{ km s}^{-1}$. Interestingly, this is comparable to the escape velocity from the Galaxy. If we assume the velocity is approximately constant during the entire evolution, the characteristic timescale for the formation of the observed structure is $t_{\text{exp}} \simeq R/v_{\text{exp}} \simeq 10$ Myr, where $R \simeq 4$ kpc is the radius of the bubbles. With the total non-thermal energy estimated above, $E_{\text{n/th}} \simeq 10^{56}$ erg, the required time-averaged jet/outflow kinetic luminosity then reads as $L_{\text{jet}} \simeq E_{\text{n/th}}/t_{\text{exp}} \simeq 3 \times 10^{41} \text{ erg s}^{-1}$, which is $\sim 0.1\%$ of the Eddington luminosity of the Sgr A* Eddington supermassive black hole. Note that these results are exactly consistent with the independent estimate by Totani (2006) as described above.

The above estimates are quite modest, and in our opinion, do not conflict with the existing observations. Yet, our arguments are not sufficiently strong to rule out the alternative conventional idea that the NPS originates from a nearby supernova remnant. Worth remarking in this respect is that the expansion velocity we derived conflicts with the order-of-magnitude higher values advocated in the literature (Guo & Mathews 2012; Guo et al. 2012; Zubovas & Nayakshin 2012; Yang et al. 2012; Lacki 2013). We note that such large expansion velocities would result in the formation of a very strong bow shock at the bubbles' boundaries, manifesting in very hot gas at the edges of the structure with temperatures of $kT \simeq 3 - 17$ keV. Currently there is no observational evidence for the presence of such a diffuse gaseous component around the Fermi Bubbles, or even within the Galaxy, except for its most central regions (≥ 5 keV plasma within ~ 100 pc of Sgr A*, the origin of which is still under debate; Koyama et al. 2007).

Finally, we note an interesting analogy between the Fermi Bubbles and the giant, relic lobes in the nearby radio galaxy Centaurus A, which have been also resolved with WMAP and *Fermi*-LAT (Hardcastle et al. 2009; Abdo et al. 2010), and for which the recent *Suzaku* observations indicated analogously a rough pressure equilibrium with the surrounding medium (Stawarz et al. 2013). In both cases, the radiating ultra-relativistic electrons were proposed to be accelerated *in-situ* via interaction with magnetic turbulence, rather than at weak shocks formed eventually at the bubbles/lobes edges. However, large-scale shock wave may anyway be required to generate turbulence accelerating high energy particles in the Fermi Bubbles (Mertsch & Sarkar 2011). Reconnecting large-scale magnetic field may also play a role in this context in the Galactic Center region (Sofue et al. 2005) as well as in

the lobes of AGN (Gourgouliatos & Lyutikov 2012). High-quality radio and X-ray observations of the Fermi Bubbles interiors, enabling a diagnosis of the plasma conditions and magnetic field structure similarly as in the case of the giant Centaurus A lobes (O'Sullivan et al. 2013; Stawarz et al. 2013) are needed to elaborate more on the particle acceleration processes at work (Cheung et al., in prep.).

5. CONCLUSIONS

In this paper we presented the results of our *Suzaku* X-ray observations of high Galactic latitude regions positioned at the edges of the γ -ray Fermi Bubbles recently discovered with *Fermi*-LAT. We showed that the detected diffuse X-ray emission is well reproduced by a three-component plasma model including unabsorbed thermal emission of the Local Bubble ($kT \simeq 0.1$ keV), absorbed thermal emission related to the North Polar Spur and/or Galactic halo ($kT \simeq 0.3$ keV), and a power-law component at the level expected from the cosmic X-ray background. We did not find a non-thermal X-ray emission component associated with the bubbles exceeding $\sim 15\%$ fluctuation of the CXB intensity, corresponding to $< 9.3 \times 10^{-9} \text{ erg cm}^{-2} \text{ s}^{-1} \text{ sr}^{-1}$ in the 2–10 keV energy range. Based on the gathered data, we argued that the North Polar Spur is possibly related to the bubbles rather than being a local phenomenon. This followed from the indirect evidence we found for the presence of a large amount of neutral matter absorbing the X-ray emission of the structure, as well as for a weak shock driven by the bubbles' expansion in the surrounding medium and compressing the halo gas to form the NPS feature. In this scenario, we estimated the expansion velocity of the bubbles as $v_{\text{exp}} \sim 300 \text{ km s}^{-1}$, corresponding to the shock Mach number $\mathcal{M} \simeq 1.5$. We also showed that the non-thermal pressure and energy estimated by means of modeling the broad-band spectrum of the bubbles in the framework of a simple one-zone leptonic model, $p_{\text{n/th}} \simeq 2 \times 10^{-12} \text{ dyn cm}^{-2}$ and $E_{\text{n/th}} \simeq 10^{56}$ erg, respectively, are in a rough equilibrium with the pressure and energy of the thermal plasma surrounding the bubble.

We acknowledge the referee for a careful reading and for a number of useful and positive suggestions that helped improve the manuscript. This work is partially supported by the Japanese Society for the Promotion of Science (JSPS) KAKENHI. We would like to thank Drs. M. Ishida and N. Yamazaki for useful discussions on the nature of the GH plasma. Ł.S. was supported by Polish NSC grant DEC-2012/04/A/ST9/00083. Work by C.C.C. at NRL is supported in part by NASA DPR S-15633-Y.

APPENDIX

X-RAY SPECTRA OF COMPACT SOURCES

As discussed in the text (Section 3.2.1), we believe that the bulk of the uncatalogued point-like X-ray features detected in our *Suzaku* observations at the $\gtrsim 5\sigma$ level are background AGN or galaxies and are unrelated to the GH or NPS structure. In this Appendix, we first summarize the positions and the statistical significances of compact X-ray features detected above 3σ , and possible association of catalogued sources when possible (Tables 3 & 4). X-ray spectral fits of uncatalogued sources detected above $\gtrsim 5\sigma$ level (with the assumed absorbed power-law model) are then summarized in Table 5.

ABUNDANCE OF THE $kT \simeq 0.3$ KEV PLASMA COMPONENT

The limited photon statistics preclude us from precisely determining the metallicity of the absorbed $kT \simeq 0.3$ keV diffuse emission component, hence we fixed $Z = 0.2 Z_{\odot}$ in the model fitting (see Section 3.2.2). To validate our assumption, in Figure 9 we plot the temperature kT versus the abundance for the N1–N8 pointings, derived when both Z and kT were allowed to vary. The derived values cluster in a relatively narrow range of $kT \simeq 0.3$ keV and $Z \simeq 0.2 Z_{\odot}$ indeed. We note the related discussion

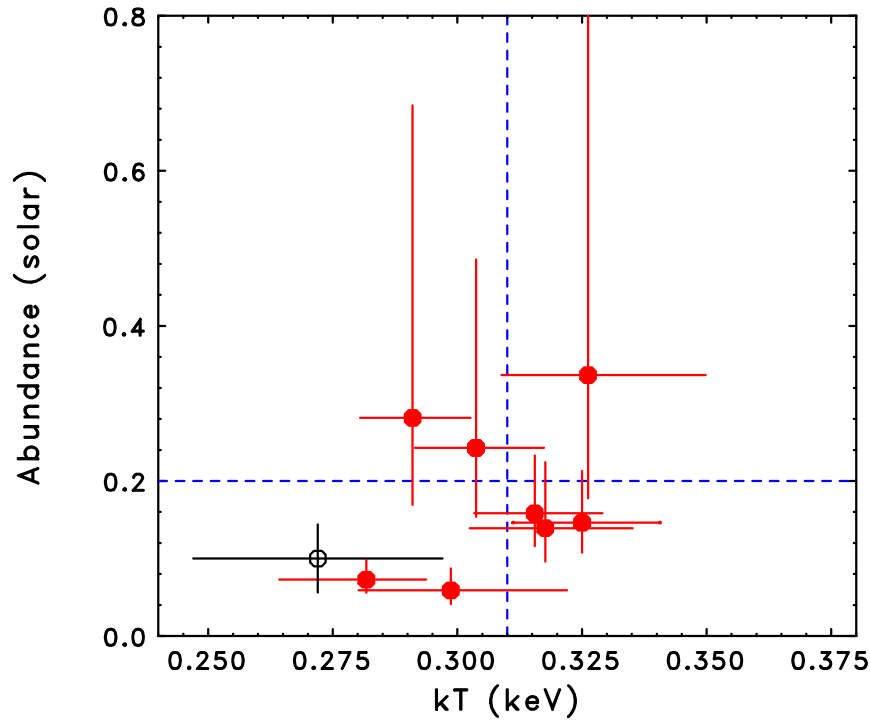


FIG. 9.— Temperature kT versus abundance Z for the diffuse X-ray emission component APEC2 in the N1–N8 fields (filled red circles) and southern fields (average over S1–S6; open circle), derived assuming the three component plasma model introduced in Section 3.2.2, but with the abundance set free in the fitting procedure. Blue dashed lines show the means of the best fit parameters, namely $kT = 0.31$ keV and $Z = 0.2 Z_{\odot}$.

in Willingale et al. (2003) and Miller et al. (2008) concerning the brightest regions of the NPS targeted by *Suzaku* and *XMM*, suggesting the depleted C, O, Ne, Mg and Fe abundances of less than $0.5 Z_{\odot}$, but an enhanced N abundance which was however not clearly seen in our data.

EM OF $kT \simeq 0.1$ KEV PLASMA

Since the XIS is only sensitive to photon energies above 0.4 keV, clearly distinguishing between the two diffuse thermal components ($kT \simeq 0.1$ keV due to the LB/SWCX and $kT \simeq 0.3$ keV due to the GH/NPS) is in general not easy. Therefore, it is in principle possible that a gradual jump visible in the derived EM between different neighboring fields (as seen in Figure 6), may be due to a sudden increase in the amount of contamination from the LB/SWCX component rather than a drop in the GH/NPS component. In order to investigate this issue in more detail, in Figure 10 we plot the variation of the EM of the $kT = 0.1$ keV plasma for the N1–N8 and S1–S6 pointings. As expected, no significant variations in the EM are observed, thus confirming the reality of a gradual drop in the EM for the $kT \simeq 0.3$ keV component claimed in Section 3.2.2.

REFERENCES

- Abdo, A. A., et al. 2010, *Science*, 328, 725
 Atwood, W. B., et al. 2009, *ApJ*, 697, 1071
 Berezhko, E. G., Völk, H. J. 2004, *A&A*, 419, L27
 Berkhuijsen, E. M., Haslam, C. G. T., & Salter, C. J. 1971, *A&A*, 14, 252
 Bingham, R. G. 1967, *MNRAS*, 137, 157
 Bland-Hawthorn, J., & Cohen, M. 2003, *ApJ*, 582, 246
 Blumenthal, G. R., & Gould, R. J. 1970, *Reviews of Modern Physics*, 42, 237
 Crocker, R. M., & Aharonian, F. 2011, *Physical Review Letters*, 106, 101102
 Day, C., et al., 1998, *The ASCA Data Reduction Guide*, Tech. Rep., (Greenbelt: NASA GSFC), 355 v.2.0
 Dickey, J. M., & Lockman, F. J. 1990, *ARA&A*, 28, 215
 Dobler, G., & Finkbeiner, D. P. 2008, *ApJ*, 680, 1222
 Dobler, G., Finkbeiner, D. P., Cholis, I., Slatyer, T., & Weiner, N. 2010, *ApJ*, 717, 825
 Egger, R. J., & Aschenbach, B. 1995, *A&A*, 294, L25
 Finkbeiner, D. P., 2004, arXiv:astro-ph/0409027
 Foster, A. R., Ji, L., Smith, R. K., & Brickhouse, N. S. 2012, *ApJ*, 756, 128
 Fujimoto, R., Mitsuda, K., Mccammon, D., et al. 2007, *PASJ*, 59, 133
 Furst, E., & Reich, W. 1990, *Galactic and Intergalactic Magnetic Fields*, 140, 73
 Giommi, P., Angelini, L., Jacobs, P., & Tagliaferri, G. 1992, in *ASP Conf. Series*, 25, 100
 Gold, B., Odegard, N., Weiland, J. L., et al. 2011, *ApJS*, 192, 15
 Gourgouliatos, K. N., & Lyutikov, M. 2012, *MNRAS*, 420, 505
 Guo, F., & Mathews, W. G. 2012, *ApJ*, 756, 181
 Guo, F., Mathews, W. G., Dobler, G., & Oh, S. P. 2012, *ApJ*, 756, 182
 Hardcastle, M. J., Cheung, C. C., Feain, I. J., & Stawarz, Ł. 2009, *MNRAS*, 393, 1041
 Hartman, R. C., Bertsch, D. L., Bloom, S. D., et al. 1999, *ApJS*, 123, 79
 Hasinger, G., Burg, R., Giacconi, R., et al. 1998, *A&A*, 329, 482
 Henley, D. B., Shelton, R. L., Kwak, K., Joung, M. R., & Mac Low, M.-M. 2010, *ApJ*, 723, 935
 Henley, D. B., & Shelton, R. L., 2013, *ApJ*, 773, 92
 Ishisaki, Y., Maeda, Y., Fujimoto, R., et al. 2007, *PASJ*, 59, 113
 Katsuta, J., Tanaka, Y. T., Stawarz, Ł., et al. 2013, *A&A*, 550, A66
 Koyama, K., Maeda, Y., Sonobe, T., et al. 1996, *PASJ*, 48, 249
 Koyama, K., Tsunemi, H., Dotani, T., et al. 2007, *PASJ*, 59, 23
 Koyama, K., Uchiyama, H., Hyodo, Y., et al. 2007, *PASJ*, 59, 237
 Kushino, A., Ishisaki, Y., Morita, U., et al. 2002, *PASJ*, 54, 327
 Krumpke, M., Lamer, G., Corral, A., et al. 2008, *A&A*, 483, 415
 Lacki, B. C., 2013, *ApJ*, submitted, arXiv:1304.6142
 Mathewson, D. S., & Ford, V. L. 1970, *MNRAS*, 74, 139
 Matsuoka, M., Kawasaki, K., Ueno, S., et al. 2009, *PASJ*, 61, 999
 Merloni, A., Predehl, P., Becker, W et al. 2012, *MPE document*, S. Allen et al., eds., arXiv:1209.3114

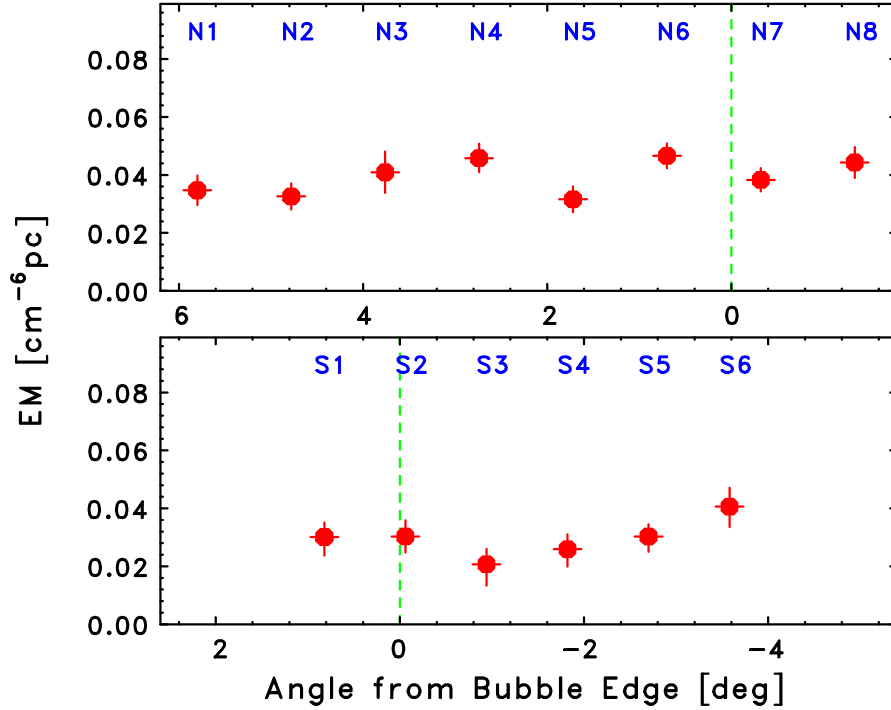


FIG. 10.— Variation in the spectral fitted EM parameter of the APEC1 emission component in the north-east (*top*) and south (*bottom*) *Suzaku* observations, as a function of the angular separation from the bubble edge. No significant changes in the EM at the expected position of the bubbles' boundary (green dotted line following Su et al. 2010) are seen, consistent with the expectation that the $kT \simeq 0.1$ keV plasma component is due to the Local Bubble emission contaminated by the solar wind charge exchange.

- Mertsch, P., & Sarkar, S. 2011, *Physical Review Letters*, 107, 091101
 Miller, E. D., Tsunemi, H., Bautz, M. W., et al. 2008, *PASJ*, 60, 95
 Mitsuda, K., Bautz, M., Inoue, H., et al. 2007, *PASJ*, 59, 1
 Murakami, H., Koyama, K., Sakano, M., Tsujimoto, M., & Maeda, Y. 2000, *ApJ*, 534, 283
 Murakami, H., Koyama, K., Tsujimoto, M., Maeda, Y., & Sakano, M. 2001, *ApJ*, 550, 297
 Nolan, P. L., Abdo, A. A., Ackermann, M., et al. 2012, *ApJS*, 199, 31
 O'Sullivan, S. P., Feain, I. J., McClure-Griffiths, N. M., et al. 2013, *ApJ*, 764, 162
 Planck Collaboration, Ade, P. A. R., Aghanim, N., et al. 2013, *A&A*, 554, A139
 Serlemitsos, P. J., Soong, Y., Chan, K.-W., et al. 2007, *PASJ*, 59, 9
 Snowden, S. L., Freyberg, M. J., Plucinsky, P. P., et al. 1995, *ApJ*, 454, 643
 Snowden, S. L., Egger, R., Freyberg, M. J., et al. 1997, *ApJ*, 485, 125
 Sofue, Y. 1973, *PASJ*, 25, 207
 Sofue, Y., Hamajima, K., & Fujimoto, M. 1974, *PASJ*, 26, 399
 Sofue, Y. 1976, *A&A*, 48, 1
 Sofue, Y. 1977, *A&A*, 60, 327
 Sofue, Y., & Reich, W. 1979, *A&AS*, 38, 251
 Sofue, Y. 1984, *PASJ*, 36, 539
 Sofue, Y. 1994, *ApJ*, 431, L91
 Sofue, Y. 2000, *ApJ*, 540, 224
 Sofue, Y. 2003, *PASJ*, 55, 445
 Sofue, Y., Kigure, H., & Shibata, K. 2005, *PASJ*, 57, L39
 Su, M., Slatyer, T. R., & Finkbeiner, D. P. 2010, *ApJ*, 724, 1044
 Su, M., & Finkbeiner, D. P. 2012, *ApJ*, 753, 61
 Stawarz, L., Tanaka, Y. T., Madejski, G., et al. 2013, *ApJ*, 766, 48
 Takahashi, T., Abe, K., Endo, M., et al. 2007, *PASJ*, 59, 35
 Takeuchi, Y., Kataoka, J., Stawarz, L., et al. 2012, *ApJ*, 749, 66
 Tawa, N., Hayashida, K., Nagai, M., et al. 2008, *PASJ*, 60, 11
 Totani, T. 2006, *PASJ*, 58, 965
 Tozzi, P., Rosati, P., Nonino, M., et al. 2001, *ApJ*, 562, 42
 Wang, Q. D., 2002, arXiv:astro-ph/0202317
 Willingale, R., Hands, A. D. P., Warwick, R. S., Snowden, S. L., & Burrows, D. N. 2003, *MNRAS*, 343, 995
 Wright, E. L., Eisenhardt, P. R. M., Mainzer, A. K., et al. 2010, *AJ*, 140, 1868
 Xiao, L., Fürst, E., Reich, W., & Han, J. L. 2008, *A&A*, 482, 783
 Xu, J. W., Han, J. L., Sun, X. H., et al. 2007, *A&A*, 470, 969
 Yang, H.-Y. K., Ruszkowski, M., Ricker, P. M., Zweibel, E., & Lee, D. 2012, *ApJ*, 761, 185
 Yao, Y., & Wang, Q. D. 2005, *ApJ*, 624, 751
 Yao, Y., Wang, Q. D., Hagihara, T., et al. 2009, *ApJ*, 690, 143
 Yao, Y., Wang, Q. D., Penton, S. V., et al. 2010, *ApJ*, 716, 1514
 Yoshino, T., Mitsuda, K., Yamasaki, N. Y., et al. 2009, *PASJ*, 61, 805
 Zubovas, K., & Nayakshin, S. 2012, *MNRAS*, 424, 666

TABLE 3

LIST OF COMPACT X-RAY FEATURES DETECTED ABOVE 3σ LEVEL AND REMOVED IN THE ANALYSIS OF DUFFUSE X-RAY EMISSION: BUBBLE NORTH

ID	R.A. [$^{\circ}$]	DEC [$^{\circ}$]	stat sig ^a (σ)	association ^b	comment ^c	
src1	233.354	9.033	10.6	—		
src2	233.286	9.159	9.1	—		
	233.304	9.098	3.7	—		
	233.503	9.015	4.5	—		
src3	233.692	8.032	4.9	—		
	233.623	8.015	4.5	—		
	233.825	7.110	4.9	—	low-E	
src4	233.825	7.110	4.9	—		
	233.933	7.175	6.2	—		
src5	233.870	7.108	3.8	—		
	233.779	7.032	4.1	—		
	233.710	7.057	4.5	—		
	233.940	7.053	3.7	—	low-E	
	233.879	7.024	7.7	Radio Source		
	233.888	6.976	16.5	QSO		
	233.773	7.129	12.0	QSO		
	233.745	7.137	4.3	Radio Source		
	src6	234.102	6.160	6.7	—	
	src7	234.001	6.120	5.7	—	
		234.100	6.101	3.3	Radio Source	
src8	234.018	6.150	4.4	Galaxy		
	233.982	6.145	4.0	Galaxy		
	234.000	6.195	3.5	Galaxy		
	234.262	5.151	3.7	—		
	234.323	5.182	4.5	—		
	234.285	5.191	4.1	—		
	234.420	4.170	5.4	—		
	src9	234.446	4.120	6.2	—	
		234.317	4.071	3.3	—	low-E
	src10	234.287	4.218	3.3	—	high-E
234.378		4.147	7.8	QSO		
234.481		3.210	5.8	—		
src11	234.478	3.252	3.3	—		
	234.725	2.243	5.3	—		
	234.837	2.149	20.2	QSO		
	234.617	2.123	15.3	QSO		

NOTE. — ^a: Statistical significance determined by the source detection algorithm in XIMAGE. Only XIS0+3 data were used since the XIS1 has lower imaging quality due to higher instrumental background.

^b: Catalogue association of the source, if available.

^c: Sources detected only in the 0.5–2 keV energy range are denoted as “low-E”, and sources detected only in the 2–10 keV energy range are denoted as “high-E”.

TABLE 4

LIST OF COMPACT X-RAY FEATURES DETECTED ABOVE 3σ LEVEL AND REMOVED IN THE ANALYSIS OF DUFFUSE X-RAY EMISSION: BUBBLE SOUTH

ID	R.A. [$^{\circ}$]	DEC [$^{\circ}$]	stat sig ^a (σ)	association ^b	comment ^c
src1	332.660	-45.883	4.8	—	
src2	332.705	-45.902	5.8	—	
	332.649	-45.758	13.7	Star	
	332.731	-45.929	6.0	Galaxy Group	
	332.723	-45.947	6.9	QSO	
src3	331.432	-45.662	4.8	—	
	331.493	-45.726	3.8	—	
	331.509	-45.664	3.8	Star	
src4	330.338	-45.613	8.3	—	
src5	330.124	-45.483	6.9	—	
	330.225	-45.423	4.0	—	
	330.227	-45.550	3.4	—	
	330.169	-45.395	5.3	Radio Source	
src6	329.014	-45.269	22.4	—	
src7	329.155	-45.310	7.1	—	
	329.096	-45.337	4.5	Galaxy	
	329.041	-45.507	10.6	Radio Source	
src8	327.788	-45.245	6.6	—	
	327.863	-45.330	3.6	Star	
src9	326.635	-45.203	4.8	—	
src10	326.653	-47.000	4.7	—	
	326.688	-45.191	3.4	—	
	326.496	-45.106	7.0	Radio Source	

NOTE. — As in Table 4, but for the sources in the south bubble observations.

TABLE 5
FITTING PARAMETERS FOR COMPACT X-RAY FEATURES DETECTED ABOVE $\gtrsim 5\sigma$ LEVEL

ID	N_{H}^a (10^{20} cm^{-2})	PL index ^b	PL flux ^c ($10^{-14} \text{ erg cm}^{-2} \text{ s}^{-1}$)	χ^2/dof
Bubble North				
src1	3.37(fix)	$2.44^{+0.23}_{-0.22}$	$6.19^{+1.70}_{-1.46}$	1.29/41
src2	688^{+619}_{-340}	$0.76^{+0.79}_{-0.60}$	$74.7^{+21.2}_{-10.5}$	1.47/31
src3	3.83(fix)	$2.41^{+0.51}_{-0.46}$	$3.96^{+2.55}_{-1.83}$	1.00/68
src4	3.86(fix)	$2.26^{+0.43}_{-0.38}$	$2.05^{+1.02}_{-0.82}$	0.79/17
src5	3.86(fix)	$3.06^{+0.71}_{-0.76}$	$0.94^{+1.30}_{-0.59}$	1.00/22
src6	4.06(fix)	$1.43^{+0.35}_{-0.33}$	$8.35^{+2.97}_{-2.61}$	1.27/17
src7	4.06(fix)	$2.06^{+0.32}_{-0.30}$	$3.22^{+1.20}_{-1.02}$	1.30/25
src8	4.45(fix)	$1.67^{+0.40}_{-0.37}$	$4.23^{+1.70}_{-1.49}$	1.07/23
src9	4.45(fix)	$2.70^{+0.52}_{-0.45}$	$1.43^{+0.95}_{-0.67}$	1.06/28
src10	4.26(fix)	$1.75^{+0.32}_{-0.30}$	$5.68^{+1.95}_{-1.70}$	0.36/13
src11	5.02(fix)	$1.40^{+0.44}_{-0.41}$	$5.59^{+2.56}_{-2.11}$	1.19/10
Bubble South				
src1	1.84(fix)	$1.72^{+0.45}_{-0.41}$	$3.82^{+1.90}_{-1.57}$	0.94/19
src2	1.84(fix)	$1.34^{+0.53}_{-0.51}$	$4.75^{+2.49}_{-2.08}$	0.25/9
src3	1.66(fix)	$1.83^{+0.52}_{-0.49}$	$3.17^{+1.91}_{-1.47}$	0.65/13
src4	1.89(fix)	$1.85^{+0.36}_{-0.33}$	$7.50^{+3.08}_{-2.60}$	0.96/18
src5	1.89(fix)	$0.93^{+0.27}_{-0.29}$	$15.1^{+3.7}_{-3.4}$	0.72/19
src6	2.16(fix)	$2.31^{+0.14}_{-0.13}$	$17.2^{+3.1}_{-2.8}$	0.98/68
src7	2.16(fix)	1.24 ± 0.33	$8.66^{+2.79}_{-2.50}$	0.98/34
src8	2.45(fix)	$1.60^{+0.29}_{-0.27}$	$6.42^{+2.07}_{-1.85}$	1.12/19
src9	3.03(fix)	$1.95^{+0.70}_{-0.65}$	$2.56^{+2.03}_{-1.48}$	0.88/7
src10	3.03(fix)	$1.60^{+0.53}_{-0.48}$	$8.88^{+5.80}_{-4.27}$	0.78/7

NOTE. — ^a: Absorption column density fixed at the Galactic values, except for src2 in the North, which required an additional column density well exceeding $N_{\text{H, Gal}}$.^b: Spectral photon index in the single power-law model.^c: Unabsorbed 2 – 10 keV flux.